RAMAN IMAGING OF COUNTERFLOW DIFFUSION FLAMES

A Dissertation
presented to
the Faculty of the Graduate School
University of Missouri-Columbia

In Partial Fulfillment
of the Requirements for the Degree

Doctor of Philosophy

---

by
SERDAR YERALAN

Dr. Joseph A. Wehrmeyer, Dissertation Supervisor

DECEMBER 1995

The undersigned, appointed by the Dean of the Graduate School, have examined the dissertation entitled

RAMAN IMAGING OF COUNTERFLOW DIFFUSION FLAMES

presented by Serdar Yeralan

a candidate for the degree of Doctor of Philosophy

and hereby certify that in their opinion it is worthy of acceptance.

Joseph A. Wehrmeyer

John B. Miles

R. C. Warder Weyden

James P. Neal

Meera Chandrasekhar

ACKNOWLEDGMENTS

I would like to take this opportunity and declare my deepest appreciation to a few individuals who have been very supportive and instrumental in my efforts during the last few years. I believe working with my advisor Joseph A. Wehrmeyer has taught me many lessons. From him, I have learned how to conduct a scientific research and carefully examine results. He has been a wonderful mentor and a friend whom I had the privilege to work with. The rest of my committee members deserve a special acknowledgment for being very supportive and thorough. I believe my efforts have met with success mainly because of the support I have received from my family and friends. My parents and siblings have continually supported me over the years and I feel very lucky to have them. I believe my parents' love and support have filled my life with happiness and laughter. I can only hope to be a parent as exemplary as they are. One of the individuals who has a special place in my life is my girlfriend, Heike Gerber. Her confidence and courage have inspired me to achieve higher goals and her support made many of my darkest moments filled with comfort. I would like to extend my thanks to some of my close friends who have helped me in many occasions. J. A. Sweet, J. P. Spicer, J. P. Hartfield, R. Hessel, B. Giangregorio, S. Barda, D. Cleary, K. Gustavson, B. Betz, B. Johnson, A. Young, O. Osbourne and A. Hagevik are some of the people with whom I have created wonderful friendships and shared unforgettable experiences. I would also like to thank my office-mates, K. S. Tecu and G. Holscher who have put up with me in the last few years. Lastly, I would like to thank the Department of Mechanical and Aerospace Engineering and NSF for funding me and my dissertation during the last four years.

RAMAN IMAGING OF COUNTERFLOW DIFFUSION FLAMES

Serdar Yeralan

Dr. Joseph A. Wehrmeyer, Dissertation Supervisor

ABSTRACT

Hydrogen versus air counterflow diffusion flames are studied with linewise Raman imaging system. Raman measurements are gathered over 20 second duration with high precision (2%) and high spatial resolution (160 μm). Axial strain rate values are measured by laser Doppler velocimetry. Three different fuel jet concentrations are studied: mole fractions of 21% hydrogen diluted with 79% nitrogen, 50% hydrogen diluted with 50% nitrogen and undiluted hydrogen. Axial strain rate is varied for each of the fuel dilution cases. Raman images of these flames are converted into temperature and major species mole fraction profiles. Mixture fraction and scalar dissipation rate profiles are generated from the mole fraction information. Strain rate and differential diffusion effects are clearly illustrated by the results. Numerically predicted strain rate and differential diffusion effects are experimentally matched. Peak temperatures values agree well with numerical estimates for all of the fuel dilutions except for the undiluted fuel jet cases. At least 50 K higher temperatures are observed for undiluted fuel jet flames when compared to numerically predicted temperatures of these flames. A library of mixture fraction and scalar dissipation rate is generated for hydrogen-air combustion.

TABLE OF CONTENTS

Chapter

Appendix

LIST OF TABLES

Table Page

LIST OF FIGURES

Figure Page

Figure Page

CHAPTER-I

INTRODUCTION

The study of combustion has been one of the defining characteristics in human civilization. From the first fires of the Neanderthals to space exploring vehicles, combustion science has shaped our lives. This thesis is one of those many efforts that hopes to aide our journey into the future where space travel is a part of daily life. The scope of this work involves developing a set of laminar strained flame data from which beneficial information may be gathered and utilized in different areas of combustion science. Resulting from this data a better understanding and simulation of turbulent flames, that play a major role in our everyday lives, is the hopeful wish of the author and his colleagues. Combustion science, as complex as it may be, can be broken down to disciplines to further our understanding. One impetus to understand hydrogen fueled combustion is associated with the National Aerospace Plane (NASP) project. This vehicle was conceptually designed to take off from a landing strip and travel at hypersonic speeds in the higher regions of the atmosphere. Supersonic combustion ramjet engines (SCRAMJET) are needed to achieve hypersonic velocities using air-breathing combustion. The only practical fuel that can be used in this combustion application is hydrogen. Thus the push in hydrogen fueled supersonic combustion studies was underway in early 1980's. Combustion scientists have realized that there is much to be benefited from hydrogen combustion science. Hydrogen is one of the most common species in our chemical energy sources. It is one of the first species to undergo some changes in hydrocarbon-fueled combustion. Thus, the more understanding of hydrogen-fueled combustion that is achieved, the better grasp on hydrocarbon reactions that is obtained.

This project aims at bringing a piece of assistance to practical problems of combustion phenomena. It is well acknowledged that combustion is a part of our lives. It encompasses many aspects of our lives. Every time a heater is turned on, or a car is started we are benefiting from the knowledge gained through combustion science. Almost all of these practical devices utilize turbulent flames to achieve their design objectives. Thus the need for better understanding, controlling and modeling of turbulent flames has emerged. Due to the extreme complexity of turbulent combustion, it is decided to use numerical models to gain insight to the phenomenon. These models vary in their structures and assumptions [Peters 1984]. One of the models that has received a great deal of attention is the "asymptotic flamelet model" [Liñán 1974]. The model, which is based on the boundary layer formulation of Prandtl [Prandtl 1904], makes use of method of matched asymptotic expansions to describe the interactions of diffusion and finite rate kinetics. This model covers a regime of turbulent flames where chemistry, compared to transport processes, is fast such that it occurs in asymptotically thin layers. These layers are given the name "flamelets" and they represent a finite-sized combustion zone embedded within the turbulent flow field.

To develop a complete set of data for numerical investigation, one may find it useful to express fundamental combustion equations in a conserved scalar domain. This reduces the number of variables to two, mixture fraction and scalar dissipation rate [Peters 1984]. Mixture fraction is an independent variable that gives a universal description to combustion [Kuo 1986]. The scalar dissipation rate of the conserved scalar represents the diffusion time scale compared to the chemical time scale [Peters 1984]. The velocity gradient of the fluids is called strain rate. Strain rate, which is strictly a function of fluid dynamics, is directly correlated with scalar dissipation rate. Researchers have derived an explicit relationship between these two important variables [Kim and Williams 1993]. It is both numerically and experimentally demonstrated that as the flame stretch, which is proportional to strain rate, increases, the scalar dissipation rate increases. If the flame stretch exceeds a critical value, the flamelet will extinguish since diffusion of the reactants require more time than what is provided by the flowfield [Chelliah et al. 1990]. The flamelet formulation works especially well in hydrogen fueled combustion since hydrogen has a chemical reaction time scale which is comparatively shorter than the convection and diffusion time scales. Thus, combustion takes place within asymptotically thin regions of the turbulent flow. In addition, counterflow diffusion burners are well suited for creating the conditions of laminar diffusion flames that can easily be represented as flamelets. The simplicity of the burner allows easy access to the flame front for measurements along with well characterized boundary conditions. The numerical challenges of combustor representation is minimized by the simple boundary conditions and the one dimensionality of the flame zone. It should also be noted that the stagnation flow field is a well studied topic in fluid mechanics [Schlichting 1955; Luna 1965]. Thus the formulation and the equations are well tested and represented.

The development of a turbulent combustion model requires a great deal of experimental verification and guidance. Many researchers have obtained temperature and species profiles of counterflow flames with intrusive probes [Pandya and Weinberg 1964; Tsuji and Yamaoka 1966]. Although these pioneering efforts contributed a great deal to the qualitative understanding of these flames, quantitative results came after the development of laser-based techniques such as Raman spectroscopy. Applications of Raman spectroscopy to combustion science are numerous [Eckbreth, Bonczyk and Verdieck 1979; Lederman 1977; Yaney et al. 1982; Drake, Lapp and Penney 1982]. In recent years charge-coupled devices (CCDs) have replaced photo-multiplier tubes as detectors allowing multi-point, multi-species Raman measurements within the combustion zone [Nandula et al. 1994; Reckers et al. 1993; Sick et al. 1990].

The goal of the current research effort is to gather a library of scalar dissipation rate and mixture fraction profiles of hydrogen-air opposed jet non-premixed flames at various strain rates. This library can be utilized to address many of the needs to enhance a hydrogen-fueled turbulent flame model. The data gathering is accomplished non-intrusively by Raman spectroscopy. A liquid nitrogen cooled CCD is utilized to obtain multi-point measurements of temperature and all of the major species concentration of hydrogen diffusion flames. An opposed jet configuration is chosen as the combustor design. Relatively simple flow field of the combustor enables easy and accurate modeling of the opposed jet flames.

In recent years, unsteady strain rate and vortex interaction effects of flamelets on combustion have been gaining interest [Katta and Roquemore 1995; Barlow and Chen 1992]. Although the current research does not address these issues, the experimental system used in this research has shown to have the capability of expanding and adequately handling these type of experimental investigations [Rolon, Aguerre and Candel 1995].

In the following chapters previous research, experimental arrangement, results, discussion of the results and some conclusions are given. A literature review of counterflow flames is placed at the start of Chapter-II. The same chapter reviews the literature of theoretical and experimental research that is relevant to hydrogen fueled counter flow diffusion flames. A literature review of laser diagnostics applied to counterflow flames is also included in Chapter-II. Starting with the burners that are used in the experiments to the Raman scattering, the overall system arrangement and the LDV set-up are explained in Chapter-III. Results and discussion of the experiments are covered in Chapter-IV. Graphs of mole fraction, temperature and mixture fractions as functions of axial location are located in this chapter. Graphs of mole fraction, temperature and scalar dissipation rate as functions of mixture fraction of atomic hydrogen graphs are also included in Chapter-IV. Chapter-V is the conclusion of the research thesis. It reiterates the important results and offers future work.

CHAPTER-II

LITERATURE REVIEW

A-COUNTERFLOW FLAMES

Interest in counterflow flames dates back to early studies of combustion of gases. Potter and Butler did a pioneering study of "flame strength" by means of determining the maximum rate of mass flux a gaseous fuel can sustain before blow-off conditions are reached in a counterflow diffusion flame between two opposing tubes [Potter and Butler 1959]. Similar studies were continued by Potter and others for a number of years [Potter, Heimel and Butler 1962; Anagnostou and Potter 1963]. These studies concentrated on determining the "flame strength" for different fuels and studying the effects of fluid mechanical parameters. They discovered that the tube diameter linearly influenced the "flame strength", as the diameter increased the "flame strength" increased. They also discovered that there is no correlation between the "flame strength" and the Reynolds number for Reynolds number less than or equal to 2000. At the same time Spalding introduced the first theoretical works of the opposed jet diffusion flames [Spalding 1961]. Using the Spalding-Zeldovich reduced scheme, Spalding was able to model Potter's experiments and predict the same results as the experimental results of Potter and his colleagues. Spalding concluded that these experiments would give insight into reaction rate constants of various fuels. Shortly after Spalding's investigation, Fendell developed a theory of ignition and extinction based on the first Damköhler number to simulate experimental studies of extinction [Fendell 1965]. Along with Potter's efforts in the field of combustion science, Pandya and Weinberg investigated flame structures in opposed jet ethylene-air diffusion flames [Pandya and Weinberg 1964]. They generated temperature profiles, gas composition profiles, flow field studies and field of refractive index studies of these flames by using thermocouples, gas chromatography, illuminated particles, and spectrometry, respectively. A new theoretical approach was developed for studying the structures of counterflow diffusion flames with large activation energies such as hydrogen fuel [Liñán 1974]. In this study the author assumed that the flame has an asymptotic structure, and divided the flame into four regimes. The first regime is the nearly frozen ignition regime where no reaction is taking place. The second regime is the regime where partial burning occurs. The third regime is the premixed flame zone. The final regime is the near-equilibrium diffusion controlled zone of the flame. The demonstration of this study is presented in terms of Damköhler number which gave many insights to researchers of the field in the following years. In the experimental end of the field, a major development was achieved by the introduction of a new kind of opposed jet burner [Tsuji and Yamaoka 1966]. This burner is still used to this date by combustion scientists. It consist of a porous cylinder which usually injects the fuel composition into a laterally flowing oxidizer stream from a nozzle. Tsuji and Yamaoka studied the extinction limits of propane and city-gas versus air. They also developed the temperature profiles across the flame zone in these combustors. The important aspect of the opposed jet burner is the geometric simplicity which makes it attractive to computer modelers.

The computer models for opposed jet burners differ in the characterization of the boundary conditions. There exists two different treatments of the boundary conditions. One treatment is simply assuming that the boundary conditions obey the potential flow conditions [Gutheil and Williams 1990]. For this type of treatment of the flow field yields to a specified axial strain rate, valid everywhere except in the flame zone. Due to the potential flow characterization of the velocity field there cannot be a vortex or rotational velocity components to the flow field at the boundaries. In the numerical study of Gutheil and Williams the authors derived a 13 step kinetic mechanism to model the opposed jet diffusion flame. They established that thermal diffusion plays and unimportant role and that the extinction strain rate increases with increasing pressure. It was also noted in their work that abrupt extinction does not occur when the air temperature reaches a critical value i.e., 1200 K at 1 atm. The other type of boundary condition treatment is a less restrictive non-potential flow condition [Kee et al. 1988]. In this alternative approach, the modeler can choose a boundary condition to have a radial velocity component. This enables a parabolic velocity profile, which is encountered in opposing tube combustors, or a plug flow velocity profile which is more common to opposing nozzle configurations. Due to their boundary condition formulation, they had to compute the radial pressure gradient at each grid point unlike the prescribed conditions found in potential flow treatment of the boundary conditions. In this numerical study, the authors computationally derived the detailed structure and the extinction limits of opposed flow, premixed methane-air flames.

There exists new challenges for combustion scientists to overcome so that the flamelet model can successfully predict the structure of turbulent diffusion flames. These new challenges are in the areas of air stream temperature dependence of the flames, the partially-premixed aspects of turbulent flames, and the unsteady strain influences upon the flame zone. The dependence of air stream temperature on extinction and ignition limits has been numerically investigated for the hydrogen-air opposed jet diffusion flames [Darabiha and Candel 1992]. Their result demonstrated that the extinction strain rate for an air jet temperature of 1000 K (~1925 s^{-1}) is ten times larger than the extinction strain rate corresponding to an air jet temperature of 300 K. They realized that as the air stream temperature increases the amount of OH increases and the amount of HO_2 and H_2O_2 decreases. The chain branching reactions are favored and chain breaking reactions are less effective. Thus they claimed that higher strain rates are achievable with increasing air stream temperature. They indicated that as the strain rate increases the heat release rate per unit flame area increases but convective and diffusive fluxes increase more rapidly, resulting in a decease in the peak temperature value until the flame can no longer exist.

The effects of dilution and pressure on extinction conditions of methane-air diffusion flames have also been studied [Chelliah et al. 1990]. In a Tsuji-type burner, by keeping the stoichiometric mixture fraction value constant, the researchers were able to study the dilution and pressure effects on extinction. Their computer model indicated that as the fuel and the air streams are diluted, the flame temperature decreased, slowing the branching reactions while the radical recombination rates remained the same. Thus extinction is achieved at lower strain rates. Extinction strain rate is found to increase with increasing pressure but less strongly at higher pressures.

A similar study was done with hydrogen fuel [Papas, Glassman and Law 1994]. The researchers were able to conduct experiments of hydrogen-air opposed jet diffusion flames at two different pressures (0.5 atm and 1.0 atm) and five different fuel dilutions. They obtained profiles of maximum flame temperature versus strain rate for different fuel dilutions. They also included pressure versus temperature profiles along with density weighted strain rate versus pressure profiles. The numerical part of this investigation was based on the work done by Smooke and his coworkers [Smooke, Puri and Seshadri 1994]. The S-shaped ignition-extinction curve of hydrogen combustion is numerically generated to study individual turning points at various pressures in opposed jet hydrogen-air diffusion flames [Kreutz, Nishioka and Law 1994]. Their finding suggested that the radical pool in these flames is too small to influence the temperature profile, thus the energy equation can be decoupled from the minor species equation. Another opposed jet diffusion flame study [Puri and Seshadri 1986], developed a computer model after experimentally studying the extinction limits of methane diluted with nitrogen versus air, and propane diluted with nitrogen versus air opposed jet diffusion flames. The computer model was based on activation energy asymptotic theories [Liñán 1974]. The extinction strain rate and the model predictions matched within 50 to 60 s^{-1}. In this study, the authors also found the limiting concentration of methane and propane as a function of strain rate. Recently, a study of partially premixed combustion conditions was presented [Li and Ilincic 1995].

They experimentally determined the effects of water spray introduction into a strained, partially premixed methane with air versus air counterflow premixed flame. They realized that the prompt NO was a dominant NO mechanism and it heavily depends on the amount of water addition. A similar experiment using identical jets of methane and oxygen creating an opposed jet premixed flame was done to study strain rate variation effects [Law et al. 1994]. By tracking the velocity of the jet centerline with LDV, and obtaining temperature and major species profiles using Raman spectroscopy, the authors argued that, unlike counterflow diffusion flames, the scalar structure and flame thickness of these flames are insensitive to strain rate. These flames cannot be extinguished by strain rate alone. Egolfopoulos [1994] has numerically studied the influence of unsteady strain rate inputs upon premixed methane-air opposed jet flames. In this research it is pointed out that the strain rate amplitudes are not as high at high frequency perturbations contrary to the low frequency perturbations for the same given sinusoidal strain rate variation. Analogy between Stoke's second problem is drawn to suggest that diffusion attenuates the amplitudes of oscillatory responses.

There has been an increasing interest in the unsteady strain effects on the combustion. Some of the interesting work is done by Rolon and his colleagues [Rolon, Aguerre and Candel 1995]. They were able to create a reproducible vortex in the opposed jet diffusion flames by means of an actuated piston pushing a volume of oxidizer gas through the combustion zone. They concluded that if the vortex was strong enough it caused a hole in the flame. If the vortex was not strong enough the flame was re-established. In the same study, they were able to give simple equations that show the relationship between the flame thickness and the strain rate. Another experimental investigation studied the effects of turbulence in counterflow diffusion flames making use of a Tsuji-type burner [Tsuji, Yoshida and Endo 1994] where a turbulent oxidizing flow burned with an opposed flow of methane or propane. They concluded that the air turbulence causes some large scale small amplitude distortions leading the time averaged flame thickness to be three times larger than its laminar counterpart. They realized that there exists a critical strain rate beyond which the flame no longer exists no matter how much fuel is injected. The critical strain rate decreased with increasing turbulence intensity. They noted that the total strain rate at which the flame extinguishes corresponds to that of laminar opposed jet diffusion flame.

Important theoretical understanding of unsteady strain effects was accomplished by Darabiha [1992] who studied two particular cases: first case was a study of step increase in the strain rate, and the second case was a study of sinusoidal input of strain rate. These two different unsteady strain inputs are numerically imposed on moderately strained and near extinction limit strained flames. The results indicated that the flame responds linearly to strain rate variations if it is far from the extinction strain rate. The cut-off strain rate fluctuations appeared to be determined by mean strain rate. Flames with sufficiently high strain rates responded non-linearly to the perturbations and appeared to be more sensitive to the low frequency disturbances. Similar studies have been done by other researchers recently [Im, Bechtold and Law 1995; Im et al. 1995]. In a purely numerical study, the authors were able to impose the same strain rate perturbations as did Darabiha [Darabiha 1992]. Their results were similar to those of latter. They found that for sinusoidal strain rate perturbation the flame zone was found to be moving asymmetrically with respect to the initial location. The theoretical works of Im, Law, Kim and Williams indicated that flame response to unsteady strain rates were controlled by two main effects. Mass flux into the reaction sheet was the controlling effect for near equilibrium flames. Finite rate chemistry effects dominated fluid mechanics effects in the near extinction strain rate flames. It must be noted that this theoretical study was done for a flame that is even thinner than hydrogen diffusion flame. Since the radical recombination zone of hydrogen flames is as thick as the diffusive transport layer, the quasi-steady reaction zone is not a valid assumption for hydrogen flames.

B-HYDROGEN FUELED COUNTERFLOW DIFFUSION FLAMES

i-Theoretical Work

Theoretical investigation of hydrogen fueled opposed jet diffusion flames offered further understanding of combustion to the researcher of the field. The structure and properties of hydrogen flames has been a focal point in the theoretical investigations. A Tsuji-type burner was numerically simulated to produce graphs of mole fraction versus mixture fraction of species [Dixon-Lewis, David and Gaskell 1986]. This research was able to show the differential diffusion effects and point out that the extinction is due to breakdown in reaction $H+O_2 = OH+O$. Dixon-Lewis and Missaghi [1988] presented a paper which became a pioneering effort to many researches to come. Once again the numerical investigation of Tsuji type burner generated graphs of major species mole fraction as a function of mixture fraction, three dimensional plots of minor species mole fraction versus mean mixture fraction versus normalized strain rate. Graphs of heat release rate and temperature as functions of mixture fraction at various strain rates were included for hydrogen/nitrogen dilution of 21%-hydrogen, 50%-hydrogen and undiluted hydrogen. Another pioneering work which concentrated on the effects of pressure and air stream temperature [Gutheil and Williams 1990]. They derived a thirteen step kinetic mechanism to predict the flame behavior well. Thermal diffusion was established to be an unimportant factor and extinction strain rate was found to increase with increasing pressure. They also determined that an abrupt extinction does not occur if the air stream temperature is above a critical value. An eleven step kinetic mechanism involving seven species was used in a different numerical study [Tangirala et al. 1990]. Another numerical study of temperature effects indicated that as temperature of the air stream increased the achievable strain rate increased [Darabiha and Candel 1992]. Trees and his colleagues were able to match their numerical simulation results to experimentally determined temperature and species profiles [Trees et al. 1994]. This represents one of the only experimental investigations of the structure of H_2-air counterflow diffusion flames, and this was for relatively small strain rates. Zhao and Isaac also studied the temperature effects and determined that heating the air stream widens the flame zone and greatly increases the mole fraction and production rate of atomic nitrogen containing species [Zhao and Isaac 1995]. In another numerical study, researchers were able to create a twenty-one step kinetic mechanism to investigate the effects of pressure and reactant temperature on ignition and extinction limits [Balakrishnan, Smooke and Williams 1995]. They concluded that thermal diffusion played an important role as the air stream temperature increased. They also realized that the ignition strain rate was sensitive to the air stream temperature.

ii-Experimental Work

Early experimental studies of hydrogen fueled opposed jet diffusion flames include the ones done by Pellett and his colleagues [Pellett et al. 1989; Pellett, Northam and Wilson 1992]. The researchers were able to determine the effects of boundary conditions on extinction and ignition by using either opposing tubes, which create parabolic velocity profile, or opposing nozzles which create near-top hat velocity profile. They obtained velocity, temperature and species concentration profiles using LDV and CARS diagnostics. Another extensive study of velocity profiles gave insight to the influences of nozzle separation distance [Rolon et al. 1991]. The researchers were able to gather axial and radial velocity profiles using the LDV technique at various nozzle separations. They showed that the velocity field was not radially uniform across the flame zone. Similar conclusions were reached by Yeo and Dancey using LDV as well [Yeo and Dancey 1991]. They were able to determine what kind of boundary conditions best described their experimental system and reached to the conclusion that the less strict non-potential flow boundary conditions represented their system best [Kee et al. 1988]. Matching the numerical simulation to experimentally determined extinction strain rate was achieved by Balakrishnan and his coworkers [Balakrishnan, Trees and Williams 1994]. They were able to produce a graph of extinction strain rate as a function of hydrogen mole fraction present at the fuel jet. The numerical and the experimental curves matched reasonably well. The latest developments in experimental hydrogen fueled opposed jet diffusion flames include reproducible unsteady strain studies [Rolon, Aguerre and Candel 1995]. By producing a reoccurring vortex in the flame zone, the authors were able to investigate vortex-flame zone interactions. They concluded that if the vortex was strong enough, a hole was created in the flame zone and the flame would be extinguished. If the vortex is not strong enough the flame would recover from the vortex interaction.

C-APPLICATION OF LASER DIAGNOSTICS TO COUNTERFLOW FLAMES

The inherent difficulty in studying hydrogen fueled flames is that the flame zone is extremely thin (sub millimeter to at most few millimeters thickness). The thin flame front makes many of the data gathering techniques unacceptable due to coarse spatial resolution. Another important aspect of any gas fueled combustion research is that, due to the physical presence of the probe, the experiment may be influenced. As it is the case for many combustion science experiments, the high temperature and strain fields outrule the usefulness of many of the probes and equipment as well. It is for those reasons that a laser based technique such as vibrational Raman spectroscopy is proven to be useful. The major interests in the field of counterflow flame studies lie in temperature and species profiles along with velocity field measurements. Velocity profiles are generally obtained by an LDV or a PIV system. Pellett and his colleagues have utilized both laser based diagnostic techniques to obtain strain rate and general velocity field information [Pellett et al. 1995]. Other researchers have used LDV for determining strain rate in their experiments [Rolon et al. 1991; Papas, Glassman and Law 1994; Law et al. 1994, Chelliah et al. 1990]. Rolon and his coworkers applied LDV to determine axial and radial strain rate at different nozzle separations. Papas and his colleagues utilized LDV to obtain axial strain rate in counterflow hydrogen diffusion flames at two pressures (0.5 atm and 1.0 atm). Law and his coworkers used this laser diagnostic technique to obtain the same information in a strained premixed methane opposed jet burner at various strain rates. In this research effort they used vibrational Raman spectroscopy to gather temperature profile across the flame front [Law et al. 1994]. Trees and his coworkers investigated H_2-air diffusion flame structure using Raman spectroscopy [Trees at al. 1995]. Li and Ilincic studied water spray effects in a partially premixed methane opposed jet flame [Li and Ilincic 1995]. The water spray droplet size, distribution and velocity information is gathered by a laser based PDPA technique. In this study the flow visualization method was done using a laser sheet created from an Argon-Ion laser operating at a low power level. Brown and his coworkers demonstrated the capabilities of UV-Raman spectroscopy to gather multi-point temperature and species concentration information [Brown et al. 1994]. One of the most involved laser diagnostics systems used CARS, 2-D LIF, UV-laser absorption spectroscopy and LDV [Sick et al. 1990]. The CARS technique was used to obtain temperature and species information along with providing calibration for LIF and absorption techniques. Techniques based on UV-laser absorption and 2-D LIF were used to obtain OH concentration. The LDV was used to obtain strain rate information in this methane versus air counterflow diffusion flame.

CHAPTER-III

EXPERIMENTAL SYSTEM

A-BURNERS

There are two different burners used in the experiments. The first burner is an opposed jet burner that is used to collect the opposed jet diffusion flame data. A schematic of half of the burner is found in Fig.1. The burner is composed of two identical parts that are coaxially placed in mirror image symmetry. Part of the burner is composed of several Swagelok fittings, an aluminum outer nozzle, a Pyrex inner nozzle, small stainless steel tube, three o-rings, and a fused silica window housing. The Pyrex nozzle is used to inject combustion gases into the stagnation plane. The aluminum nozzle which encapsulates the Pyrex nozzle is to introduce low flowrate nitrogen to shield the combustion zone from the ambient air. As the figure indicates, the inside diameter of the nozzle exit is 5.0 mm. To keep the separation to nozzle diameter ratio equal to one the two identical parts of the opposed jet burner are separated by 5 millimeters. This ratio of unity results in a more stable flowfield, hence laminar flame conditions are achieved [Luna 1965]. Great care is taken such that the laser beam path coincides with the axial center line of the opposed jet burner. This procedure insures that the circular flame zone is pierced at the exact center by the laser beam. It is also a design parameter to place the focal point of the laser beam where the flame front is located.

The second burner is a Hencken burner. This burner is needed to complete the calibration of Raman signals. As Fig.2 indicates, the burner is composed of small air and fuel tubes interspersed in a honeycomb matrix located in the middle section of the burner surface. The outer annulus is a pack of small tubes issuing inert gas. The middle section of the burner and the outer annulus is divided by a stainless steel ring. The air and fuel jets create many small diffusion flames right at the burner surface. The inert gas at the outer periphery acts as a shield from ambient air. The Hencken burner is designed to reduce any kind of heat transfer back to the burner surface, thus operating at nearly adiabatic conditions [Barlow et al. 1989]. By changing the flowrates of air and hydrogen, different mole fraction ratios are achieved. To complete the calibration of the Raman signals, the temperatures of these different flames at post flame zones, thus reducing the catalytic effects, are measured by several bead diameter Pt30%Rh vs Pt6%Rh thermocouples. Using the method described by Nicholls, radiation corrected temperatures are established [Nicholls 1900]. Further details of temperature measurements are explained in Appendix A. After the temperatures and the flowrates of air and hydrogen are noted, the STANJAN program is used to compute the mole fractions of H_2, HO, H, O_2, O, N_2, NO, and H_2O [Reynolds 1986]. Since only major species have enough number density for Raman detection, the mole fractions of only H_2, O_2, N_2, and H_2O are used to calibrate the Raman signals. This completes the calibration procedure for the Raman spectroscopy since now there are available Raman signals of major species at different temperatures which correspond to known mole fractions.

B-RAMAN SCATTERING

i-Theory

Before the Raman effect can be explained, it is instructional to understand the energy storage modes of a molecule or an atom. One can explain the ways that a molecule or an atom stores energy through quantum mechanics, which shows that energy is stored by different means. The total energy of a molecule is composed of its translational energy, vibrational energy, rotational energy, and its electronic energy. A diatomic molecule is a good example to study these different energy modes. The translational energy of a molecule is a result of the motion of the particle. The kinetic energy of a molecule is due to its speed and finite mass. The rotational energy of a molecule is also due to kinetic energy but the source of the kinetic energy is the rotation of the molecule about an axis. Since the space is three dimensional, the molecule can rotate about one of these three axes. Two atoms of a diatomic molecule are constantly vibrating back and forth. This vibration of the atoms is responsible for the vibrational energy of the molecule. Vibrational energy is due to the kinetic energy of the vibrating atoms and the potential energy associated with the intermolecular force. A spring with two masses attached at the ends make a good model for understanding the vibrational energy mode. It is easily understood that compression and tension of the spring is a way to store potential energy. The pure vibrational motion of the molecules constitutes the kinetic energy portion of the vibrational energy storage mode of a molecule. There are electrons in motion around the nuclei of the atoms that make up the molecule. These motions of the electrons create kinetic energy due to shear translational movement, and potential energy due to the location of these electrons in the electromagnetic force field created by the nuclei. This is called the electronic energy of the molecule.

Raman scattering is a way to alter the rotational and/or the vibrational energy level of a molecule or an atom. When coherent light interacts with a molecule or an atom it momentarily alters the dipole moment orientation. This change results in the shift of the vibrational energy level of the molecule if the energy of the coherent light source is matched. The molecule reaches a virtual vibrational energy level for a very brief moment and emits a photon to return to its original state that is more stable. In this translational period, the molecule might emit a photon that is at exactly the same wavelength as the coherent light source. This process is called Rayleigh scattering. The molecule may also emit a photon that is at a higher wavelength and return to a vibrational state that is above its original state. This process is called Stokes Raman scattering. Likewise, it may emit a photon that is at a lower wavelength and return to a vibrational state that is below its original state. This is called anti-Stokes Raman scattering. Raman scattering is perhaps best explained by Fig.3, which represents the vibrational quantum levels.

The first prediction of the Raman effect dates back to 1878 [Lommel 1878]. Lommel predicted that when light interacts with matter, there would be light emission of frequencies at fundamental vibrational frequencies away from the incident frequency. Mathematically, the two wavelengths can be written as:

$$(\nu_o \pm \nu_v) \qquad (3\text{-}1)$$

where, ν_o refers to the incident light and the ν_v refers to the molecule's fundamental vibrational frequency. Later, Raman scattering was explained by a quantum mechanical treatment [Smekal 1923]. Smekal had learned from Einstein's photon hypothesis that the energy of a photon can only be at discrete values. In other words, the energy of the photon is quantized and it is related to the frequency of the photon by:

$$E=h\nu \qquad (3\text{-}2)$$

where h is the Planck's constant. Smekal realized that the energy of the incident photon and the energy of the molecule must be conserved at all times. Since the internal energy of the molecule can only be at quantized amounts the scattered photon energy can only be at discrete values. He derived the following way to describe the energy of the scattered photon:

$$(\nu_o \pm \Delta E/h) \qquad (3\text{-}3)$$

where the ΔE represents the initial and the final energy of the molecule. The first experimental observation of the phenomenon was made by C. V. Raman in 1928 [Raman

1928; Raman and Krishnan 1928]. Because of his discovery, the scattering process was given his name. In 1923 K. R. Ramanathan, who was one of Raman's students, conducted an experiment where he directed an intense sun beam through a color glass filter onto a purified sample of water. He found a faint trace of different color scattered light. After careful examination, Raman and his students declared that they were observing what is today called the Raman scattering. After lasers became widely available, researchers realized Raman spectroscopy as an excellent measurement tool for species and temperature. The working equations are explained in detail in Appendix B. There it is shown how one can relate Raman signal intensity to the number density of the scattering molecules.

ii-Overall Arrangement

As mentioned in Chapter-I, the goal of this study is to collect a library of scalar dissipation rate and mixture fraction profiles of hydrogen-air opposed jet non-premixed flames at various strain rates. The method of gathering the information is Raman spectroscopy.

Referring to Fig.4, the scattering process is achieved by a Q-switched neodymium-yttrium-aluminum-garnet (Nd:YAG) laser. The laser's radiation wavelength is 1064 nm. The laser beam is passed through a frequency doubling crystal, therefore the operational wavelength is reduced to 532 nm. The output beam of the laser contains a combination of 1064 nm and 532 nm laser radiation. A wavelength separation package provided with the laser is utilized to separate the two different frequencies and the 1064 nm radiation is blocked by a beam stop. The only Raman excitation radiation is 532 nm. The laser provides bursts of temporally and spatially coherent photons of 5 to 7 ns duration. The bursts occur at 10 Hertz and have 300 mJ of average energy per laser pulse. The laser beam is focused such that the beam waist reduces from 7 mm to about 0.5 mm in diameter in a 0.75 m distance by an anti-reflection coated focusing lens. The focused beam goes coaxially through the nozzles and pierces the flame. The very middle of the flame that is pierced by the laser beam is magnified and focused onto the entrance slit of the imaging spectrometer, which is 1.8 cm long and 2.0 mm wide. Due to the magnification ratios of the collection optics (M=2) and the internal magnification of the spectrometer (M=1.3), the resultant magnification of the entire optical system is 2.6. The exit of the spectrometer is where the liquid nitrogen cooled CCD detector is placed and focused. The CCD chip is made up of electron wells that are about 25 µm wide, and there is about 2 µm space between each well. There are 256 wells that are perpendicular to the spectrometer's wavelength dispersion axis, and 1024 wells that are parallel to the spectrometer's wavelength dispersion axis. Therefore, the imaged section of the flame is only 2.5 mm wide. These electron wells of the CCD chip can be binned to create bigger size pixels known as super pixels. The current project is conducted such that the CCD chip is binned by 8 pixels in the axial direction and binned by 20 pixels in the wavelength direction. Thus resulting in a compromise between spatial resolution and Raman signal strength. The spatial resolution is about 160 µm. The superpixel size contributes 80 µm of the spatial resolution. Finite laser beam waist (500 µm) decreases the spatial resolution by an additional 60 µm. Moreover, aberrations in the optical system decreases the spatial resolution to total of 160 µm. This experimental arrangement allows linewise Raman imaging of the flame.

It is also important to note that this liquid nitrogen cooled CCD has a high dynamic range (16383 counts) and low dark noise that is useful in experiments of low signal intensity. High dynamic range allows signal integration to be done directly on the chip for a long period of time and results in high accuracy (2% uncertainty).

One of the unique aspects of the experiments is the use of a ferroelectric liquid-crystal light valve (FLC). This device is composed of a swichable liquid-crystal quarter waveplate and two polarizers sandwiching the quarter waveplate. When a 5 volt current is applied to the FLC, the quarter waveplate assumes its orientation allowing vertically polarized light to pass through. The majority of the Raman signals have the same polarization as the incident light beam, which is vertically polarized. During the operation of the FLC, the Raman signals go through the first vertically oriented polarizer, pass through the liquid-crystal quarter waveplate, which rotates them 90 degrees, and exit out of the second horizontally oriented polarizer. The Raman signals suffer from high background noise levels and discriminating against this noise is achieved by fast gating of FLC. This device is 40% transmissive to the wavelength region of the experiments during its open state. The FLC is gated to have 40 μs of effective open state which results in higher signal to noise ratio than if only the chopper wheel or the mechanical shutter of the CCD camera is used [Wehrmeyer, Yeralan and Tecu 1995a]. The chopper wheel serves two purposes: firstly, it is a device to synchronize all the electronic delay/gate systems, secondly it acts as a permanent block against the background radiation while the FLC is in its opaque state and is only 0.03% transmissive. The chopper wheel rotation frequency results in an open state duration of 1.2 ms while the mechanical shutter can be open for as little as 38 ms. Thus the background luminosity is reduced by a factor of about 1.2 ms/{40 μs+0.03x(1.2 ms-40 μs)} by using the FLC rather than chopper wheel alone. It is also experimentally determined that this system results in about a 40% improvement in signal-to-noise ratio compared to an intensified CCD counterpart [Wehrmeyer, Yeralan and Tecu 1995a].

The opposed jet burner configuration shown in Fig.1 is chosen to create the laminar diffusion flame. A schematic of the flow configuration is given in Fig.5. Because the fuel nozzle Lewis number is less than unity, the flame resides on the air side of the stagnation plane. The benefits of this particular burner are that its flow field is easily modeled and it is relatively easy to build and maintain. Interest in opposed jet flows started quite some time ago. An extended fluid mechanics study of the flow configuration was done as a Ph. D. dissertation by R. E. Luna [Luna 1965]. He discovered that there is an inherent unsteadiness to the flow and he explained the unsteady nature of the configuration by perturbation theory. He argued that the stability of the stagnation plane is a function of the separation distance and the diameter of the nozzles. Instability in the stagnation plane is observed when L/D>1.5 where L is the separation distance and D is the diameter of the nozzles.

The experiments are conducted to cover three dilution ratios of the fuel for a given strain rate. These dilution ratios are 79% nitrogen, 50% nitrogen and 0% nitrogen (or undiluted fuel) at the fuel nozzle. To achieve a better stability, thus reducing the averaging effect of the moving flame in the measurements, the nozzles are separated by 5 mm. The ratio of the distance between the nozzles and the diameter of the nozzles is unity which allows a steady combustion zone. After the Raman images of the flame at different conditions are obtained, a calibration procedure that uses a Hencken burner is done in order to relate Raman signal strength of combustion species at different temperatures to the number density of the same species. This is done by simply separating the opposed jet burner nozzles by approximately 2.5 cm to allow the Hencken burner to be placed in between. The burner is placed such that the focused laser beam intersects the post flame zone exactly above the lateral center line of the burner. After obtaining mole fractions of gas species present at a given location in the flame, the ideal gas assumption is invoked to determine temperature at that location.

C-LDV SYSTEM

Laser Doppler Velocimetry (LDV) is used to obtain axial velocity profiles of the opposed jet flames. A schematic of the system is shown in Fig.6. A continuous wave argon-ion laser, operating at 514 nm with 1 Watt output, is used. The optical system consists of a polarizer, a beam splitter (TSI model 9115), an acousto-optic modulator (Bragg cell, TSI model 9182-2A), a convergent lens with a focal length of 25 cm at the beam emitting end. At the receiving end, the optical system is composed of a receiving lens with a focal length of 25 cm and a photomultiplier tube (TSI model 9140). The laser beam goes through the polarizer and the beam splitter. After the beam splitter, one beam enters the Bragg cell, which is controlled by a frequency shifter set to 10 MHz (TSI model 9186A). The frequency shifting caused by the Bragg cell discriminates directionality of the scattering particles in the control volume. The other half of the beam goes through the focusing lens and meets its counter part at the control volume. Data is gathered in an ellipsoidal control volume that has a major axis of 1.36 mm and a minor axis of 0.13 mm. The air and fuel streams are seeded with alumina (Al_2O_3) particles that have a nominal diameter of 1 μm. The particles are dried at 300 degrees Fahrenheit for 24 hours, to reduce moisture effects, and introduced into fuel and air flows via particle seeders. At the receiving end of this forward scattering LDV system all the beams coming out of the Bragg cell are blocked by a beam stop. The unshifted laser beam is collimated by a lens and directed onto PMT. The scattered light fringes made by the particles in the control volume result in a signal from PM tube. This signal is gathered by the signal processor (TSI model 1980B) and displayed on an oscilloscope. The output of the signal processor is fed into a Macintosh IIfx computer running the LabVIEW 2.0.6 program. The LabVIEW program indicated the mean and rms velocity at the control volume.

Not all of the Raman experiments were recreated and examined with the LDV system. Table 1 indicates all of the experiments. There are three boxes and each box contains four columns. The first three columns indicate the flow rate of air, hydrogen and nitrogen respectively. The last column of each box indicates the strain rate for the given flow rates. The strain rates with an asterisk are the ones that are measured by the LDV system. After these flame conditions are investigated an apparent linearity between the strain rate and the flowrates enabled the rest of the experiments to take on a strain rate value. A linear relation between the air jet flow rate and LDV strain rate values became obvious, and was used to calculate the strain rate values of experiments that are not investigated by LDV.

Q_{air}, L/min	Q_{H2}, L/min	Q_{N2}, L/min	a s^{-1}	Q_{air}, L/min	Q_{H2}, L/min	Q_{N2}, L/min	a s^{-1}	Q_{air}, L/min	Q_{H2}, L/min	Q_{N2}, L/min	a s^{-1}
X_{H2}=0.21 X_{N2}=0.79				X_{H2}=0.50 X_{N2}=0.50				X_{H2}=1.0 X_{N2}=0.0			
0.85	0.21	0.79	380^*	0.81	0.59	0.58	390	1.17	2.26	0.00	490^*
1.06	0.26	0.97	470	1.04	0.73	0.73	500	1.34	3.14	0.00	550
1.27	0.31	1.15	560	1.70	1.20	1.20	800	1.85	4.00	0.00	740
1.47	0.36	1.35	650	2.65	1.88	1.86	1250^*	2.04	5.79	0.00	810^*
1.73	0.42	1.58	760	3.47	2.42	2.41	1620	2.12	7.71	0.00	860
1.95	0.47	1.77	860	4.27	2.98	2.99	1970	2.36	8.54	0.00	1000
2.11	0.52	1.91	930	5.15	3.62	3.66	2350^*	2.73	9.86	0.00	1240^*
2.40	0.59	2.15	1050^*	6.57	4.74	4.66	2930				
2.63	0.64	2.37	1160	6.85	4.75	4.73	2960				
2.84	0.70	2.57	1250	7.67	5.40	5.31	3230				
3.03	0.75	2.73	1330	9.13	6.43	6.43	3650				
3.21	0.79	2.90	1410	9.81	6.81	6.76	3830^*				
3.54	0.86	3.20	1550								

Table 1.--Hydrogen, nitrogen, and air volumetric flowrates, and resultant strain rate.

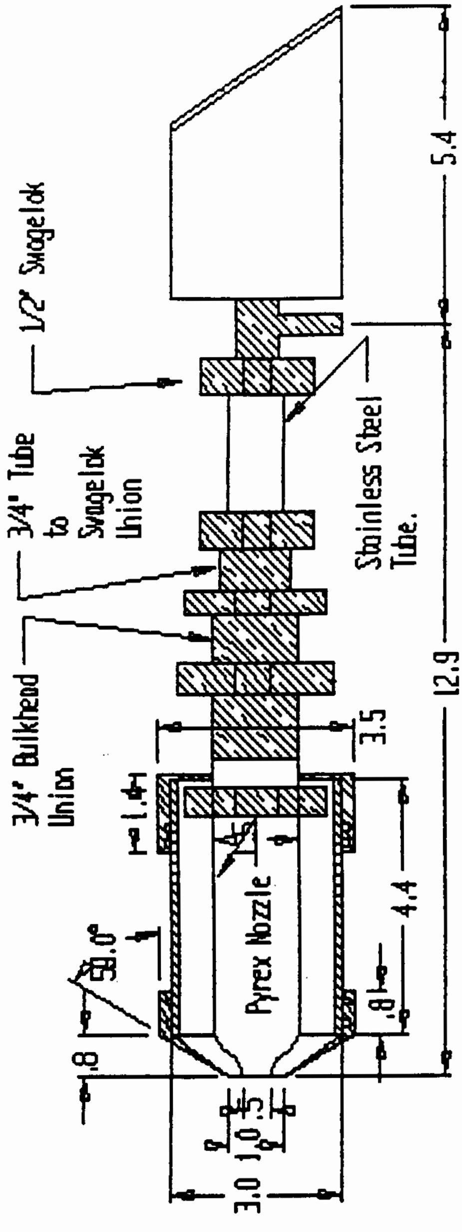

Fig.1 One side of the opposed jet burner.

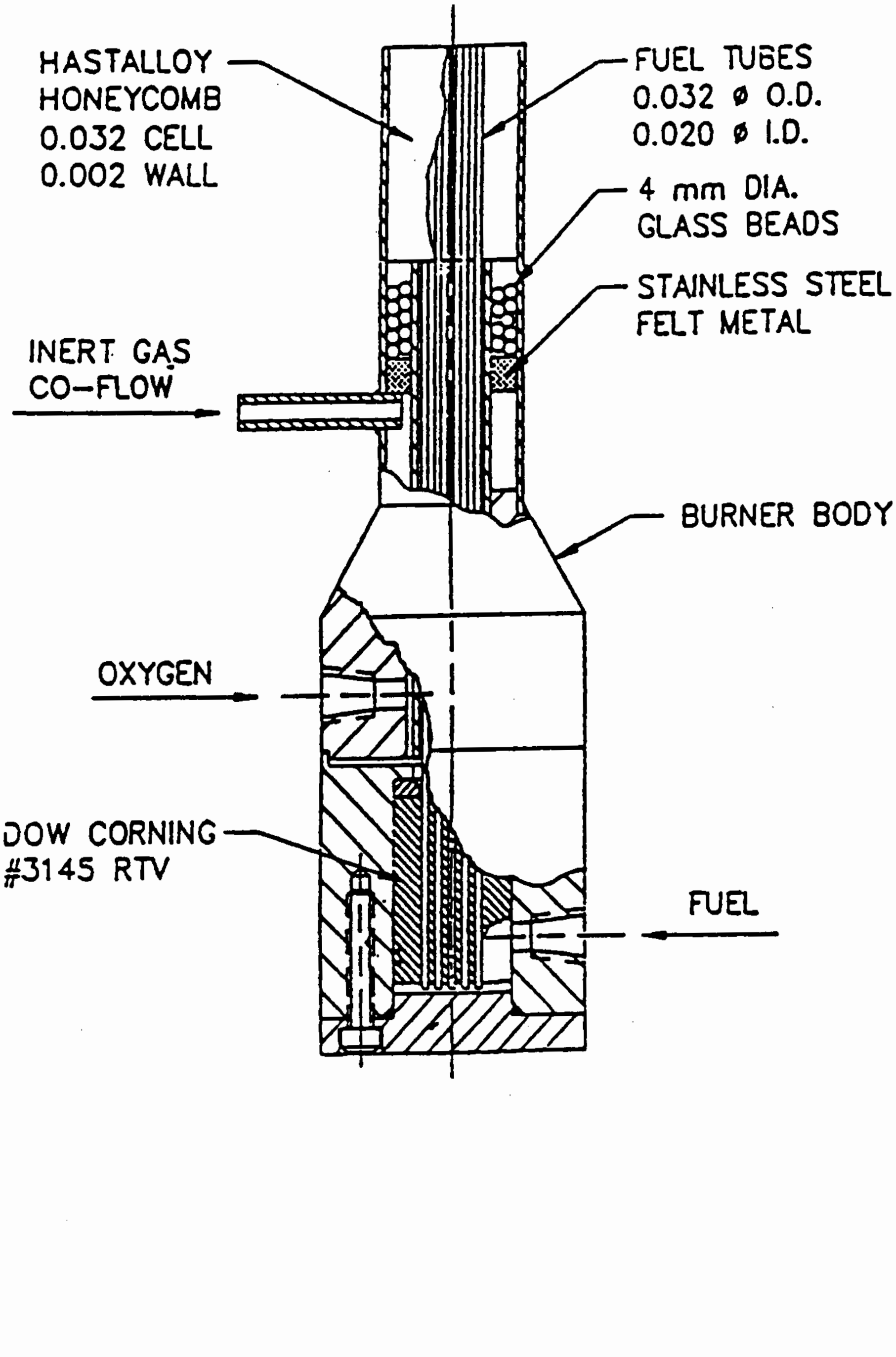

Fig.2 Cut-away view of Hencken burner.

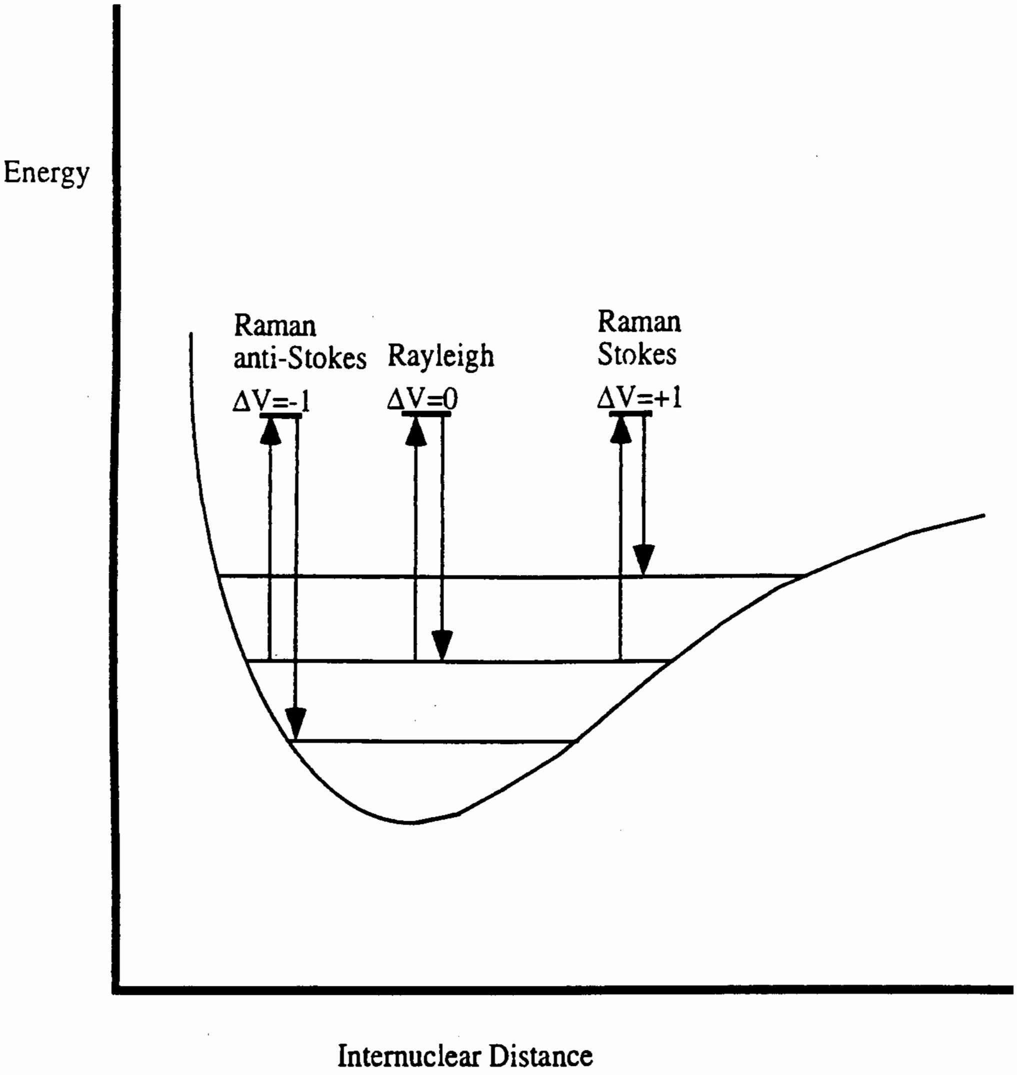

Fig.3 Light scattering processes.

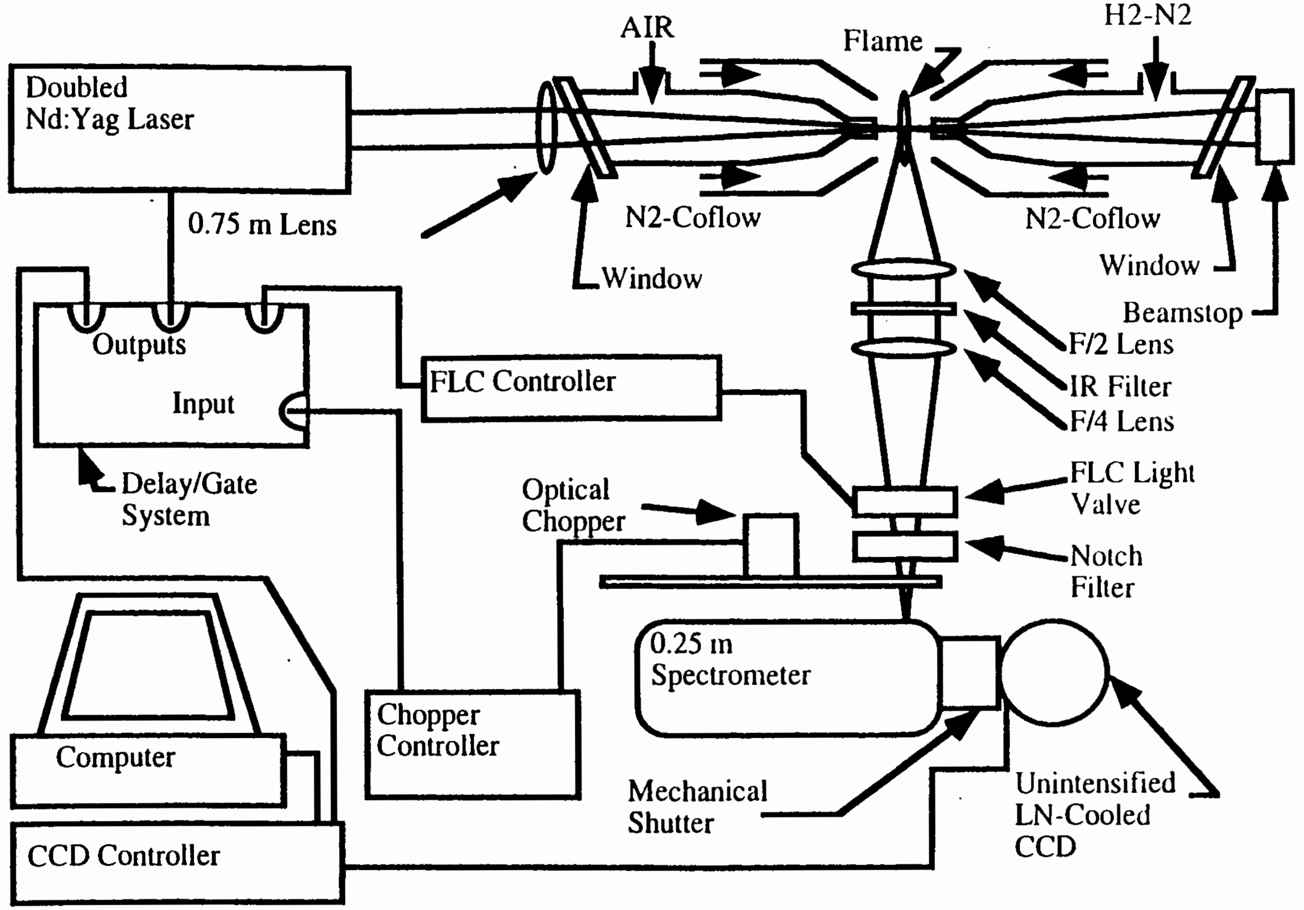

Fig.4 General experimental set-up.

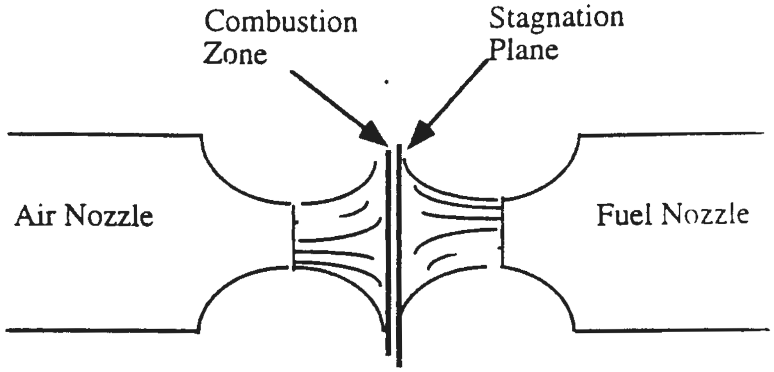

Fig.5 Opposed flow configuration.

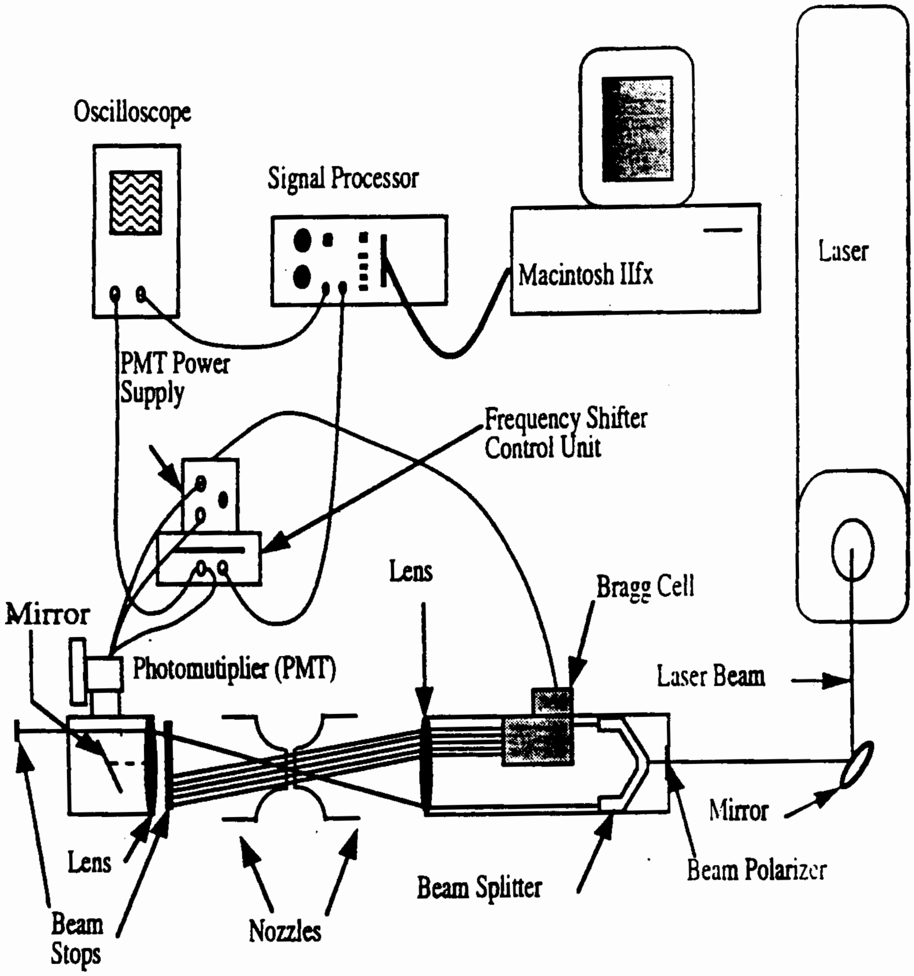

Fig.6 LDV system schematic.

CHAPTER-IV

RESULTS AND DISCUSSION

A-RAMAN DATA

The most immediate result from linewise Raman imaging is a three dimensional figure. An example of this raw data is shown in Fig.7. This figure is attained from an opposed jet diffusion flame caused by 6.8 L/min hydrogen mixed with 6.8 L/min nitrogen versus 9.8 L/min air. It is shown that raw Raman signals of the opposed jet flame can be described by three axes. One of the three axes corresponds to the axial dimension of the flame zone. The flame is located in the middle of the two nozzles and is imaged onto the spectrometers entrance slit. The exit of the spectrometer houses the CCD chip. The physical size of the chip that is perpendicular to the dispersion axis of the spectrometer is 6.4 mm. Because the Raman image of the flame is magnified by 2.6 through the lenses (M=2) and the spectrometer (M=1.3), only 2.5 mm of the flame front is imaged onto the CCD. Pixels are binned by 8 to produce 32 superpixels which results in 80 μm per superpixel in the flame front. Combination of the superpixel size, 500 μm diameter beam waist, and optical aberrations results in total spatial resolution of 160 μm. A second axis gives the wavelength information. The other dimension of the CCD (25.6 mm) corresponds to the spectral dispersion axis of the spectrometer. The 600 groove/mm grating results in 5.47 nm/mm linear dispersion, which relates to 0.14 nm/pixel and since superpixel size is 20 pixels, the resultant spectral resolution becomes 2.73 nm/superpixel. The third dimension of the graph represents the Raman signal counts. The high dynamic range of liquid nitrogen cooled CCD is apparent since the peak signals are at 3500 counts and the background noise level is at 10 counts. Figure 7 illustrates a typical scenario of an opposed jet flame. Hydrogen approaches from the edge of the imaged axis and monotonically decreases to zero value. Oxygen shows a similar trend except that it is introduced from the other side of the imaged axis. Since nitrogen is present in both the fuel and the oxidizer streams, it shows a trend that mimics both hydrogen and oxygen. Due to high temperatures and low densities, nitrogen signals drop to a minimum at the flame location. Between the hydrogen and the oxygen signals, one finds the water vapor signal. This location marks the flame zone and the high temperatures are expected to be at this location.

To relate species Raman signal strength to mole fraction values, calibration is required. As Eq. B-5 of Appendix B indicates, Raman signal count can be broken down to:

$$N_i = n_i K_i f_i(T) \tag{4-1}$$

where N_i is Raman signal intensity of species i, n_i is the number density of species i, K_i is a constant that accounts for effective efficiency of the system, and $f_i(T)$ is a temperature dependent function that accounts for the spectral dependence of species i to temperature. Raman signals of species at different temperatures are obtained by using the adiabatic calibration burner. These different temperatures are obtained via different combinations of air and hydrogen flowrates and measured by several Pt30%Rh vs Pt6%Rh thermocouples. Different bead diameters allowed radiation correction to the temperature measurements as explained in Appendix A [Nicholls 1900]. Control volume of the measurements are located in the post flame zone to reduce catalytic effects of hydrogen to the thermocouple beads. The known temperature measurements and flowrates of reactants are used as input to the STANJAN program to compute number densities of species [Reynolds 1986]. Once $f_i(T)$ and K_i are determined, a temperature is assumed and number densities for all the major species are calculated. From the number densities of species, mole fractions of species are calculated. If the mole fractions of all the major species add up to unity then the assumed temperature is correct. If the mole fractions of all the major species do not add up to unity then a new temperature is assumed. Fig.8 displays the result of the calibration procedure. Temperature and mole fraction values of species are chosen to be graphed as a function of atomic hydrogen mixture fraction which is defined as:

$$\xi_H = \frac{Y_H - Y_{H,O}}{Y_{H,F} - Y_{H,O}} \qquad (4\text{-}2)$$

where Y refers to mass fraction of hydrogen and subscripts O and H refer to mass fraction of hydrogen at the oxidizer and fuel streams, respectively. To a good approximation the above equation can be calculated as:

$$\xi_H \approx \frac{2X_{H_2} + 2X_{H_2O}}{2X_{H_2} + 18X_{H_2O} + 32X_{O_2} + 28X_{N_2}} \times \frac{2X_{H_2,F} + 28X_{N_2,F}}{2X_{H_2,F}} \qquad (4\text{-}3)$$

where the subscript F refers to the fuel jet exit conditions. Equation 4-3 also assumes initially no elemental hydrogen in the oxidizer stream. The close agreement between calculated and measured mole fraction and temperature values of calibration flames indicates the systems capability. Both the measured and calculated values have error bars associated with them. The flowmeters generally introduce 1% uncertainty to the calculated values while signal shot noise contributes 2% uncertainty to the measured values.

Once the calibration of the system is done, all of the raw opposed jet flame data can be reduced to mole fraction and temperature profiles. Two sets of such profiles are shown by Fig.9. This graph shows mole fractions of major species of two hydrogen diffusion flames at two different strain rates and corresponding temperature profiles as a function of axial down the axis of symmetry of this flame. The strain rates of these two flames are 3830 s^{-1} and 1250 s^{-1}. Both of these flames are created by equimolar concentrations of hydrogen and nitrogen versus air. Figure 9 shows many characteristics of hydrogen opposed jet diffusion flames. The expected trends of decreasing temperature and water peak values with increasing strain rate is readily observable. It is also apparent that, as the strain rate increases, more leakage of hydrogen and oxygen through the combustion zone occurs. Another expect trend is the observation of an increase in hydrogen and oxygen profile gradients with increasing strain rate. Another expected result, which is shown in Fig.9, is the thinning of the temperature and water profiles with increasing strain rate.

Temperature profiles of Fig.9 are obtained by the ideal gas assumption once number densities of each species are calculated. As Appendix B indicates, temperatures can be deduced from the ratio of Stokes to anti-Stokes Raman signal intensity. To demonstrate this capability of the experimental system, a temperature profile for a single opposed jet flame is obtained by both methods. The spectrometer is tuned to a different wavelength to capture both Stokes and anti-Stokes Q-branch nitrogen Raman signals. The resultant raw data is illustrated by Fig.10. The flowrates for this flame are: 4.7 L/min air versus 3.3 L/min hydrogen and 3.3 L/min nitrogen. To convert the raw data of Raman Stokes and anti-Stokes signals of nitrogen, the calibration burner is used in a similar manner as described above. Several calibration flame conditions with corresponding Stokes and anti-Stokes nitrogen Raman signal ratio are used to produce the calibration graph displayed in Fig.11. The best fit straight line passes has a slope of 2849 K which is approximately 85% of the calculated characteristic vibrational temperature of nitrogen, 3354 K. This can be explained by the experimental difficulty due to limited spectral range of the spectrometer which unables full capture of the Stokes nitrogen signal. As the temperature increases, vibrational Q-branch Raman signals originating from the short wavelength side increases. Since the spectral range does not include 15% of the short wavelength end of the Stokes signal, a slight decrease in sensitivity occurs at high temperatures. A comparison between two methods of obtaining temperature is illustrated by Fig.12. Uncertainties in temperature obtained by the Stokes, anti-Stokes ratio of Raman signals is about 6%. The highest discrepancy between the two methods occurs on the air side of the profile. This can partially be explained by the influence of minor species. The ideal gas law method of determining temperature assumes that only the major species are present. It is numerically shown that minor species such as H, O, and OH make up about 3% of the total number density near the peak temperature location [Dixon-Lewis and Missaghi 1988]. Thus approximately a 50 K overprediction of temperature is expected from the ideal gas law method of deriving temperature at the location of high temperature values.

Mixture fractions of the species can be graphed as a function of axial location once the mole fractions of the major species are determined. This is done by utilizing Eq. 4-3 which assumes that the minor species contribute negligible amounts to the mixture fraction. Figures 13, 14 and 15 give examples of such graphs for three different flame conditions that refer to three different hydrogen concentrations at the fuel nozzle. The first graph represents an equimolar concentration of hydrogen diluted with nitrogen versus air flame that has a strain rate of 3830 s^{-1}. Besides hydrogen, mixture fraction profiles of other two elements, namely nitrogen and oxygen, are also shown in this graph. The mixture fraction profiles for the other two elements are obtained in similar fashion. Once again Eq. 4-2 is used and approximated by major species mass fractions only. It is interesting to observe the differences in these three elemental mixture fraction profiles. Figure 13 shows that the hydrogen mixture fraction profile differs from the other two profiles indicating the effect of differential diffusion of hydrogen compared with the other heavier elements. On the air side of the flame both nitrogen and oxygen mixture fraction profiles dip into negative values due to differential diffusion of H_2O with respect to N_2 and O_2. On the fuel side of the peak temperature location which is around 1.2 mm, the three mixture fraction profiles intersect. Between this intersection point and the rest of the fuel side of the flame, the hydrogen mixture fraction profile is below the other two profiles. This is caused by the faster diffusion of hydrogen compared to the other two elements. In addition, the nitrogen mixture fraction profile achieves values above unity on the fuel side of the flame. These "overshoots" of nitrogen and oxygen mixture fraction profiles are numerically expected to occur for opposed jet flames [Dixon-Lewis and Missaghi 1988].

The same numerical investigation indicated that if the hydrogen is diluted 79% with nitrogen the monotonic behavior of the hydrogen mixture fraction profile no longer exists. This is indeed the trend in Fig.14 which corresponds to a flame condition of this dilution and strain rate of 1050 s^{-1}. This "S-shaped" curve of hydrogen mixture fraction profile indicates the differential diffusion of hydrogen compared to other species. Small characteristic "overshoots" of nitrogen and oxygen mixture fraction profiles of Fig.13 is numerically predicted to occur for this flame condition are not observed due to the experimental noise level. Larger than unity values of hydrogen mixture fraction at the fuel nozzle exit is caused by higher than indicated flowrates of hydrogen. This error is within the specifications of the flowmeter.

Undiluted fuel versus air flame of 1240 s^{-1} strain rate mixture fraction profiles as a function of physical space are illustrated in Fig.15. Assuming equal diffusivities, the stoichiometric mixture fraction value of hydrogen for this flame is 0.0283. This value corresponds to an axial location of near 0.7 mm. The three mixture fraction profiles exhibit differential diffusion effects on the lean side of stoichiometry. For example, the nitrogen mixture fraction profile first rises above hydrogen mixture fraction profile between the axial locations of 0.1 and 0.3 mm and then drops below it between 0.4 and 0.7 mm. Between the locations of 0.4 and 0.6 mm the oxygen profile is below the hydrogen mixture fraction profile and then rises above both the hydrogen and nitrogen mixture fraction profiles. Although these trends are numerically predicted, they are predicted to happen at much lower strain rates [Gutheil and Williams 1990]. The systematic error in the calibration of Raman signals is believed to be the reason for the discrepancy between the profiles at high values of mixture fraction. The hydrogen rotational Raman line S(11) occurs at 609 nm for this system. This causes interference in nitrogen vibrational Q-branch Stokes signal (at 607 nm). Thus for pure fuel flames where there is excess hydrogen present, this interference results in a measurement of slightly higher (2%) values of nitrogen. Hence the systematic error in the mixture fraction profiles for pure fuel flames.

Temperature and Mole Fraction Profiles in Mixture Fraction Space

Once the elemental species mixture fractions are determined they can then be used as substitutes for the physical space coordinate to plot mole fraction of major species and temperature as functions of mixture fraction. Because mixture fraction is a conserved scalar, results of one experiment expressed in terms of mixture fraction are readily comparable to other experimental results.

i-21% Hydrogen Case

It is apparent from Fig.14 that there is a non-monotonic behavior to the hydrogen mixture fraction profile. Using the atomic hydrogen mixture fraction as the independent variable to graph temperature and mole fractions results in erroneous representation due to this non-monotonicity. Therefore, a simple weighting of mixture fractions of the three elements has been preferred as the independent variable [Dixon-Lewis and Missaghi 1988]. A mean mixture fraction which overcomes the non-monotonicity of the elemental hydrogen mixture fraction profile is:

$$\xi_M = \frac{\xi_O + \xi_N + 3\xi_H}{5} \tag{4-4}$$

In the following figures, plots generated from four flames that correspond to the highest and the lowest strain rate along with two intermediate strain rates are taken as examples.

The first graph, Fig.16, shows temperature versus mean mixture fraction. It should be noted that the stoichiometric mixture fraction value for this case is ~0.61 assuming equal diffusivity. That value of mixture fraction corresponds to the maximum temperatures of the four plots. It is also apparent from Fig.16 that the major differences in temperature among the four plots also occur at around the mixture fraction value of 0.61. Figure 17 represents the molecular oxygen mole fraction in mean mixture fraction space. All four curves linearly decrease from their peak value of 0.21 to zero between mixture fraction value of zero and 0.61. They continue to remain zero for the rest of the range. This trait of molecular oxygen mole fraction profiles approaching zero toward the rich side of stoichiometric value of mean mixture fraction has been predicted for CO/H_2 flames [Drake and Blint 1989]. The strain rate influence is more apparent in Figs. 18 and 19 where water and hydrogen mole fractions are graphed as a functions of mean mixture fraction. As the strain rate increases, the peak water mole fraction value decreases. Hydrogen mole fraction profiles of the four flames indicate that as the strain rate increases, the breakthrough of hydrogen into the flame zone increases. At the location of stoichiometry, the flame with the lowest strain rate has mole fraction of 0.02 while the flame with the highest strain rate has mole fraction of 0.05.

ii-Equimolar Hydrogen Case

For this fuel jet case there exists a monotonic hydrogen mixture fraction profile in physical space. Thus it is used as the independent variable. Once again four representative cases, two of which correspond to the highest and lowest strain rates, are taken as examples. Figure 20 displays temperature versus hydrogen mixture fraction. The similar traits of Fig.16 are observed in Fig.20. The stoichiometric mixture fraction value of 0.304 corresponds to the peak temperature location for all four plots. The maximum difference in temperature for these four flames also occur at the location of stoichiometry. It is also observable that since the fuel jet is dilute than for the previous case, the peak temperature value of Fig.16 for 380 s^{-1} strain rate case is about 200 K less than what is demonstrated in Fig.19 for 390 s^{-1} strain rate case. Figure 21 illustrates oxygen mole fraction versus hydrogen mixture fraction. The four curves linearly decrease from their peak value of 0.21 at the oxidizer stream to zero between mixture fraction of zero and ~0.40. The stoichiometric value of 0.30 is less then 0.40 indicating that differential diffusion effects increase the mixture fraction at which the oxygen mole fraction approaches zero. It is also apparent that with increasing strain rate there is a greater oxygen breakthrough. The mole fraction of oxygen is 0.03 for the lowest strain rate flame and is 0.05 for the highest strain rate flame at stoichiometric conditions. The following two figures represent the influence of strain rate on water and hydrogen mole fraction. As was the case for Figs. 18 and 19, Figs. 22 and 23 show that with increasing strain rate there is a decrease in the peak water mole fraction value. Figure 23 shows that as strain rate increases, there is more breakthrough of hydrogen through the combustion zone.

iii-Undiluted Hydrogen Case

The following four figures represent the temperature and mole fraction of major species in hydrogen mixture fraction space. The maximum achievable strain rate (1240 s^{-1}) was limited by the high limit of the hydrogen mass flowmeter. The graphs are composed of four representative plots that correspond to highest, lowest, and two intermediate strain rate conditions. Though the highest strain rate is much less than the extinction strain rate (~8000 s^{-1}), the figures represent the characteristic strain induced effects upon the flame structure [Dixon-Lewis and Missaghi 1988; Gutheil and Williams 1991].

Figure 24 illustrates the temperature profiles of four different undiluted opposed jet flames of various strain rate. As was the case with Figs. 16 and 20, as strain rate increases peak temperature value decreases. The inset of Fig.24 demonstrates that the highest strain rate case has a peak temperature of 1950 K and the lowest strain rate case has a peak temperature of 2350 K. These values are about 100 to 300 K higher than what has been predicted by Gutheil and Williams [Gutheil and Williams 1991]. Numerical predictions done by Dixon-Lewis and Missaghi [1988] indicate temperature values that are about 50-100 K less than the experimental values. Figure 25 indicates oxygen mole fraction as a function of mixture fraction. It is observed that the oxygen mole fraction profiles start at their peak value of 0.21 at the oxidizer stream and linearly decrease to zero. Once again, the inset of the figure clearly shows the strain rate influence around the stoichiometric value of 0.0283. For the highest strained flame the mole fraction value of about 0.05 is obtained while the lowest strained flame has a value of nearly zero at stoichiometric location. Figure 26 shows that as the strain rate increases the peak water value decreases. For the highest strain rate, the peak water value is about 0.275 and climbs to a value of about 0.29 for the lowest strain rate case. The hydrogen mole fraction profiles as functions of elemental hydrogen mixture fraction are demonstrated by Fig.27. Once again it is observed that as strain rate increases form 490 to 1240 s^{-1} mole fraction of hydrogen increases from about 0.05 to about 0.1 indicating greater reactant breakthrough.

Graphs of Scalar Dissipation Rate in Mixture Fraction Space

Scalar dissipation rate is computed by the following equation [Muss, Dibble, and Talbot 1994]:

$$\chi_H = 2D(\frac{d\xi_H}{dx})^2 \tag{4-5}$$

where x is the axial coordinate, ξ_H is the elemental hydrogen mixture fraction and D is the multicomponent diffusion coefficient. Binary diffusion coefficients that are used to calculate the multicomponent diffusion coefficient are obtained from the CHEMKIN transport package, which is applicable in the range between 300 to 5000 K. Further details about the multicomponent diffusion coefficient can be found in Appendix D. After calculating multicomponent diffusion coefficients for H_2 and H_2O the following equation is used to calculate the elemental hydrogen multicomponent diffusion coefficient:

$$D(H,Mix) = \frac{D(H_2,Mix)X_{H_2} + D(H_2O,Mix)X_{H_2O}}{X_{H_2} + X_{H_2O}} \tag{4-6}$$

The numerical differentiation of the mixture fraction profile is computed using a five point central differencing technique. Thus the spatial resolution of scalar dissipation is coarser than the spatial resolution of the major species, temperature and mixture fraction measurements. However, this is needed to provide relatively smooth profiles of scalar dissipation rate.

i-21% Hydrogen Case

Figure 14 illustrates scalar dissipation rate as a function of axial location. It is observed that the peak value of scalar dissipation plot occurs at ~1.3 mm, which is at the stoichiometric value of hydrogen mixture fraction (0.61) assuming equal diffusivities. Figure 28 shows the scalar dissipation rate of mean mixture fraction as a function of mean mixture fraction that is calculated as indicated by Eq. 4-4. The replacement of elemental hydrogen based mixture fraction by mean mixture fraction reduces the fluctuations in the scalar dissipation profile due to the monotonic profile of the mean mixture fraction curve.

It is observed that as the strain rate increases from about 380 s^{-1} to 1050 s^{-1} the scalar dissipation value also increases from about 365 s^{-1} to 875 s^{-1}. The peak values of all the scalar dissipation rate curves occur around mean mixture fraction value of 0.4, which is slightly on the air side of the flame zone.

ii-Equimolar Concentration of Hydrogen Diluted with Nitrogen

Figure 13 indicates a similar trend as Fig.14 where the maximum scalar dissipation rate (~1000) coincides with the location (~1.1 mm) of stoichiometric hydrogen mixture fraction value (0.304). Once again the scalar dissipation calculation based on elemental hydrogen is plotted as a function of atomic hydrogen mixture fraction for Fig.29. It is indicated that as the strain rate increases the scalar dissipation rate increases. The peak values of the scalar dissipation rate for a given strain rate is less than its more diluted counterpart. For example the scalar dissipation rate of about 100 s^{-1} for 390 s^{-1} strain rate is observed for the equimolar case and its counterpart has scalar dissipation rate of about 360 s^{-1} at the strain rate of 380 s^{-1} for hydrogen diluted by 79% nitrogen flame.

iii-Undiluted Hydrogen Flame Case

It is as observed in Fig.30 that as the strain rate increases the scalar dissipation rate increases as well. There is a relative minima at around stoichiometric mixture fraction location for the lower strain rate flames. This trait is theoretically predicted for $CO/H_2/N_2$ flames for much lower strain rates [Drake and Blint 1988]. This dip is not predicted to occur above strain rate values of 400 s^{-1}.

LDV Data

The strain rates of the opposed jet diffusion flames are determined by laser Doppler velocimetry (LDV). The resultant velocity profiles indicate typical opposed jet flame structure where there is a distinct S-shape to the axial velocity curve. Figure 31 illustrates the axial velocity profiles of the two flame conditions that are displayed in Fig.9. The radial mean and rms values for these measurements were below 0.1 m/s along the center line. The axial rms values were as well below 0.1 m/s for these measurements except near the stagnation region where data rate is generally lower. Figure 32 demonstrates a similar velocity profile for the flame condition that is illustrated in Fig.14. The higher hydrogen dilution (79%) results in lower peak temperatures thus the velocity profile of Fig.32 indicates less significant dip than what is presented in Fig.31. The opposite trends are observed in Fig.33. This undiluted fuel flame of Fig.15 illustrates that the higher hydrogen concentration emphasizes the local maxima in the velocity profile. In addition a broader flame zone is demonstrated.

Thermophoretic influences need to be considered with LDV measurements in opposed jet flames [Sung, Law and Axelbaum 1994]. Typical particle velocities due to thermophoretic influence is in the order of a few cm/s. This velocity is comparatively small to the velocities of the opposed jet flame experiments, which are typically of the order of a few m/s at the location where strain rate is determined. In addition, the location where strain rate values are gathered is on the air side of the flame and the thermophoretic effects are much less influential at this location then they are in the combustion zone. Therefore, these LDV measurements are not corrected for the thermophoretic effects. It should be noted that the axial location of the velocity profiles are completely irrelevant to one another since they all have different zero reference locations.

After gathering LDV measurements of flames that are indicated by an asterisk in Table 1, a linear relationship between theoretically and experimentally determined strain rate values is observed. The proposed equation is used to determine theoretical strain rate values that are indicated in Table 2 [Seshadri and Williams 1978]:

$$a = \frac{2(-u_O)}{L}[1 + \frac{u_F}{(-u_O)}\sqrt{\frac{\rho_F}{\rho_O}}] \qquad (4\text{-}7)$$

where u is nozzle exit velocity, ρ is density, L is separation distance between two nozzles, and subscripts F and O refer to fuel and oxidizer streams. The following table indicates a comparison between the theoretically and experimentally determined strain rate values. This table is devised in a similar fashion as for Table 1. Three compartments are designated for the three different fuel stream compositions that are investigated. The first compartment is for the experiments that have 21% hydrogen and 79% nitrogen as fuel stream. The second compartment is for the experiments that have equimolar concentration of hydrogen and nitrogen as fuel stream. The final compartment is for experiments that use undiluted hydrogen as the fuel stream. Each block has three columns. The first column is the theoretically determined strain rate which uses Eq. 4-6. The second column is the experimentally determined strain rate. This column is the same as what is found in Table 1. The final column is the ratio of theoretical to experimental value of strain rate. It is readily observable that the ratio of theoretical to experimental value of strain rate is generally 1.6. Similar result has been obtained by Chelliah and his colleagues for methane diluted by nitrogen opposed jet flames [Chelliah et al. 1990].

The authors suggest that the differences between the strain rate values obtained by Eq. 4-6 and LDV measurements are due to the key assumptions made in deriving Eq. 4-6. Equation 4-6 is derived by assumption that the Reynolds number is large and that the mixing layer is a thin sheet located at the stagnation plane. Inviscid rotational flow with plug flow boundary conditions were used in deriving the above equation. The authors suggest that in actuality, the boundary conditions are not well represented by either plug flow or the potential flow configurations. They also indicate that there is a relatively thick mixing layer. Similar arguments apply to the discrepancy between the theoretically and experimentally determined strain rate values of Table 2.

Theo s^{-1}	Exp s^{-1}	Theo/Exp	Theo s^{-1}	Exp s^{-1}	Theo/Exp	Theo s^{-1}	Exp s^{-1}	Theo/Exp
X_{H_2}=0.21		X_{N_2}=0.7	X_{H_2}=0.5		X_{N_2}=0.5	X_{H_2}=1.0		X_{N_2}=0.0
614.5	380^*	9	618.4	390	1.6	678.4	490^*	1.4
		1.6						
757.7	470	1.6	777.07	500	1.6	885.1	550	1.6
900.9	560	1.6	1276.1	800	1.6	1154.5	740	1.6
1053.0	650	1.6	1986.1	1250^*	1.6	1565.5	810^*	1.9
1233.5	760	1.6	2573.5	1620	1.6	2035.3	860	2.4
1383.5	860	1.6	3181.1	1970	1.6	2254.8	1000	2.3
1498.1	930	1.6	3874.9	2350^*	1.7	2603.5	1240^*	2.1
1691.8	1050^*	1.6	5000.4	2930	1.7			
1858.9	1160	1.6	5056.5	2960	1.7			
2015.9	1250	1.6	5694.6	3230	1.8			
2145.7	1330	1.6	6840.4	3650	1.9			
2275.7	1410	1.6	7236.1	3830^*	1.9			
2506.9	1550	1.6						

Table 2.--Comparison of theoretical and experimental strain rates.

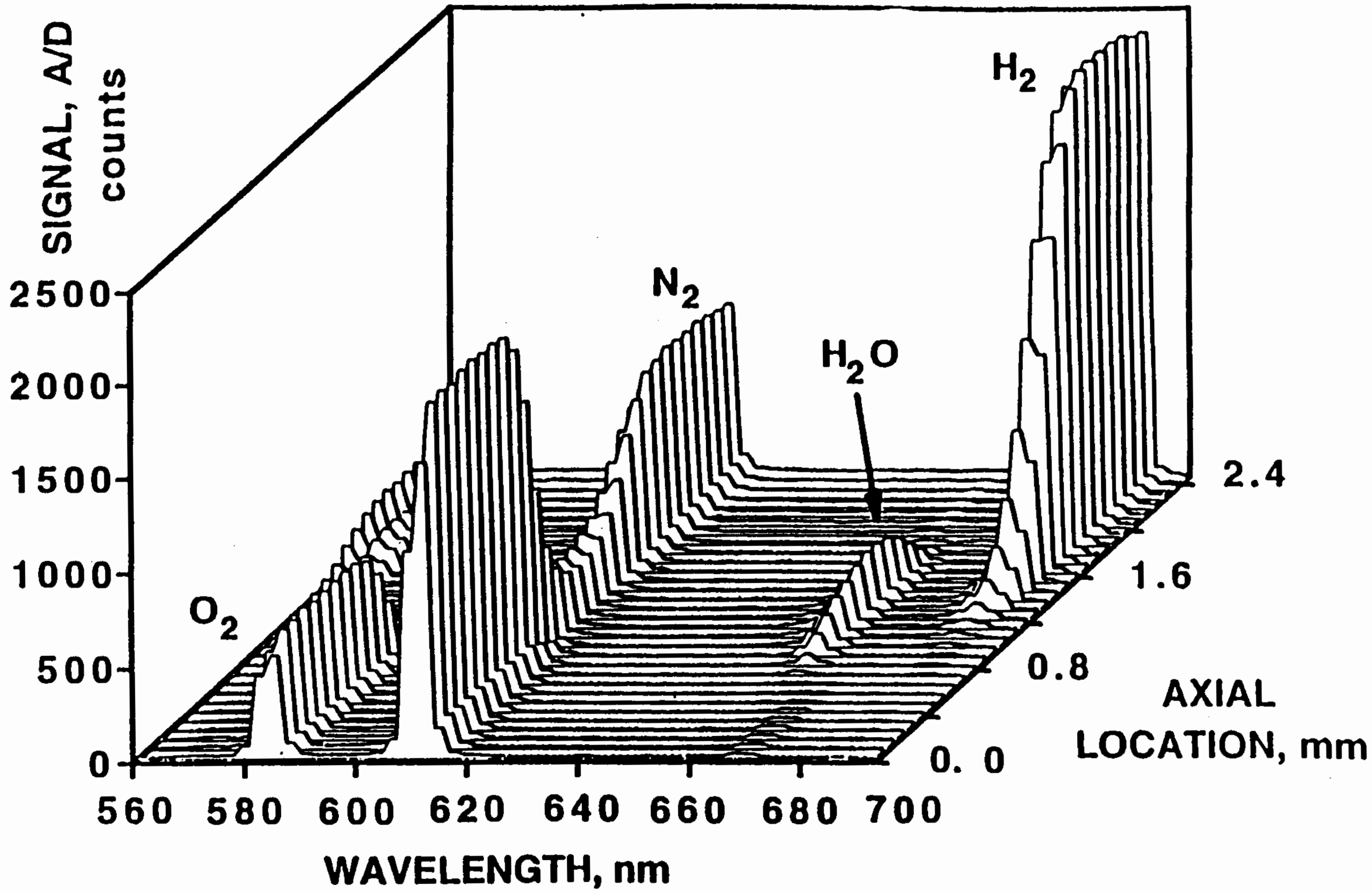

Fig.7 Opposed jet flame Raman spectra: X_{H_2}=0.5, X_{N_2}=0.5, a=3830 s^{-1}.

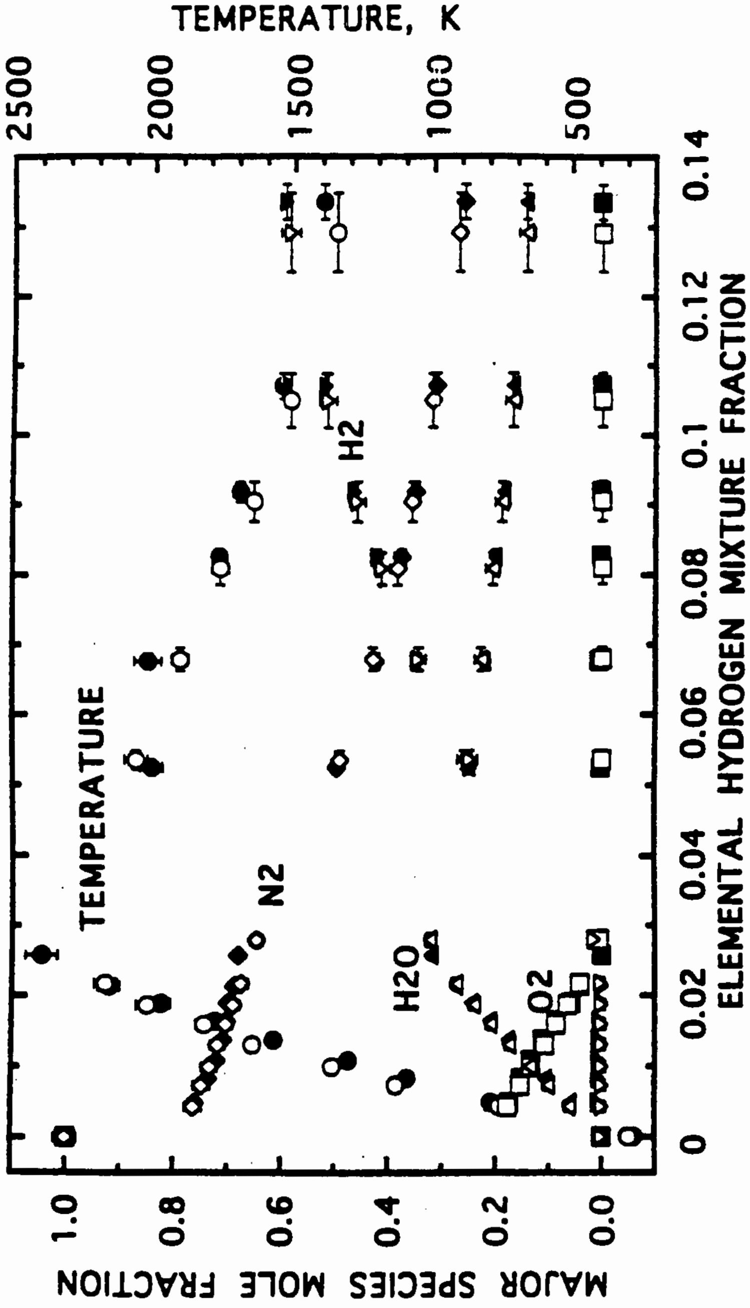

Fig.8 Raman system calibration data. Filled symbols indicate Raman data, open circles indicate calibration data.

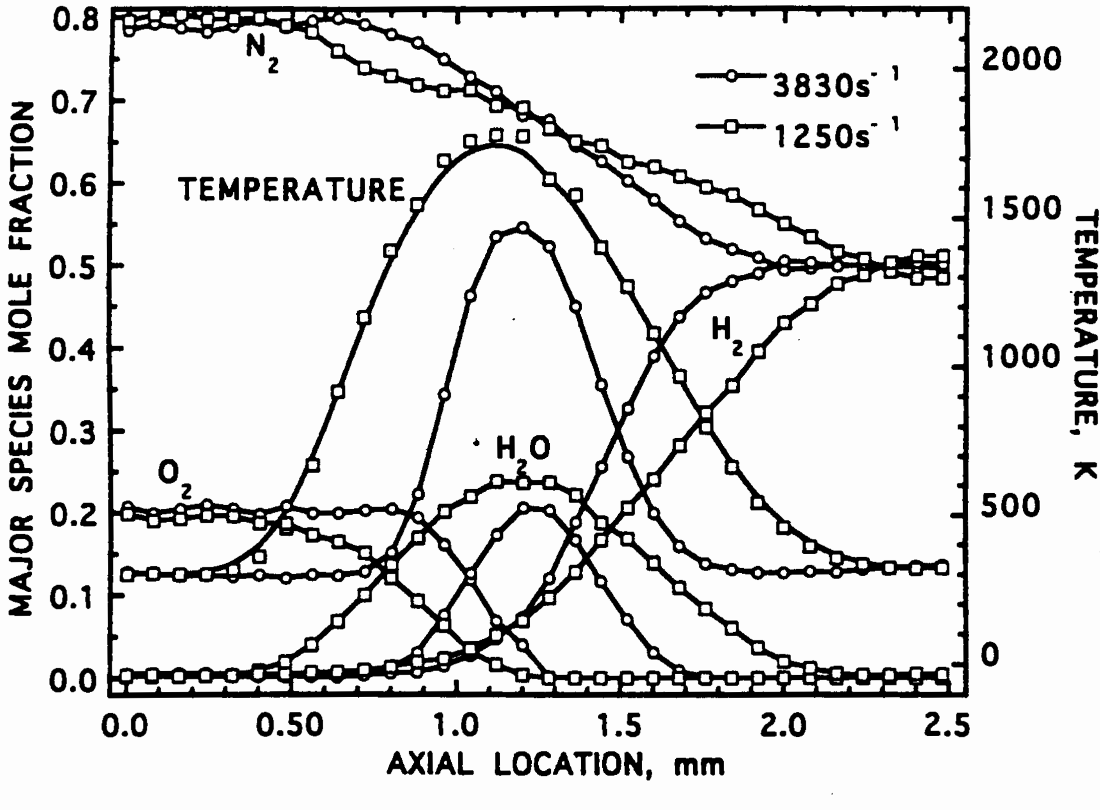

Fig.9 Mole fraction and temperature profiles of two equimolar H_2/N_2 vs air flames of different strain rates as a function of physical space.

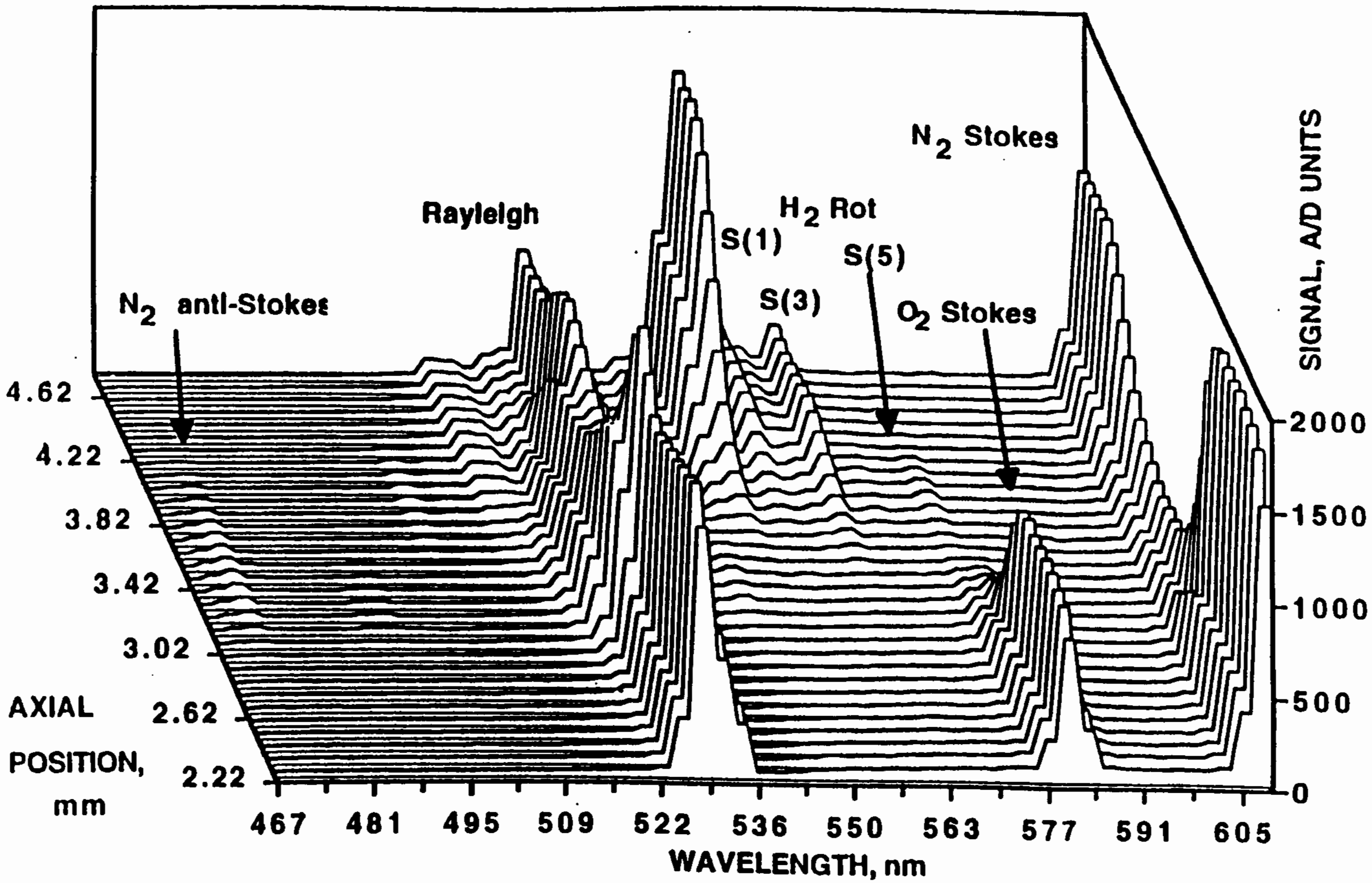

Fig.10 Stokes anti-Stokes opposed jet Raman spectra: $X_{H_2}=0.5$, $X_{N_2}=0.5$, $a=2160\ s^{-1}$.

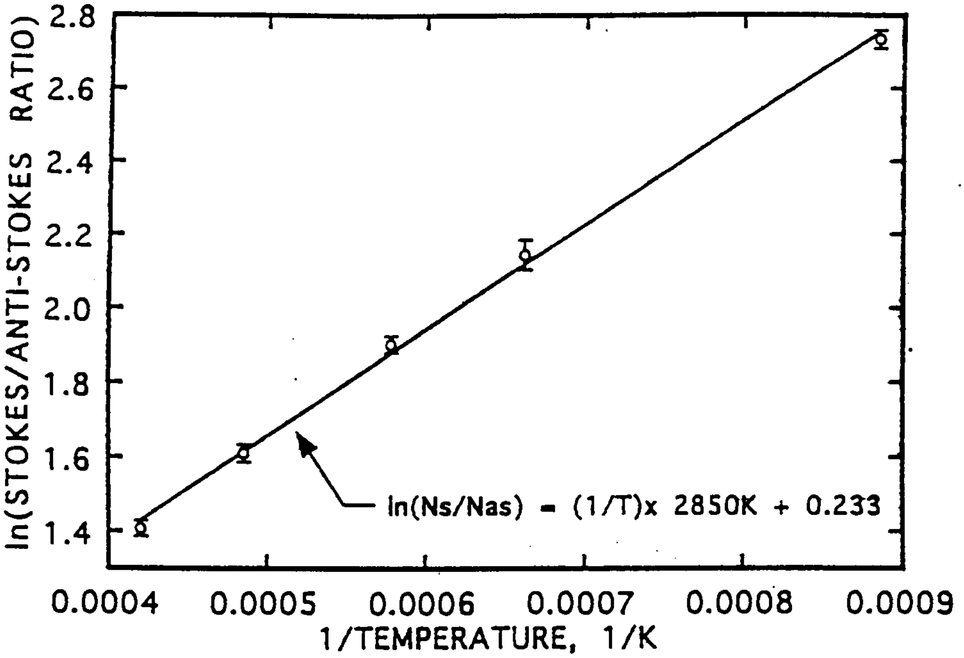

Fig.11 Calibration curve of Stokes/anti-Stokes temperature measurements.

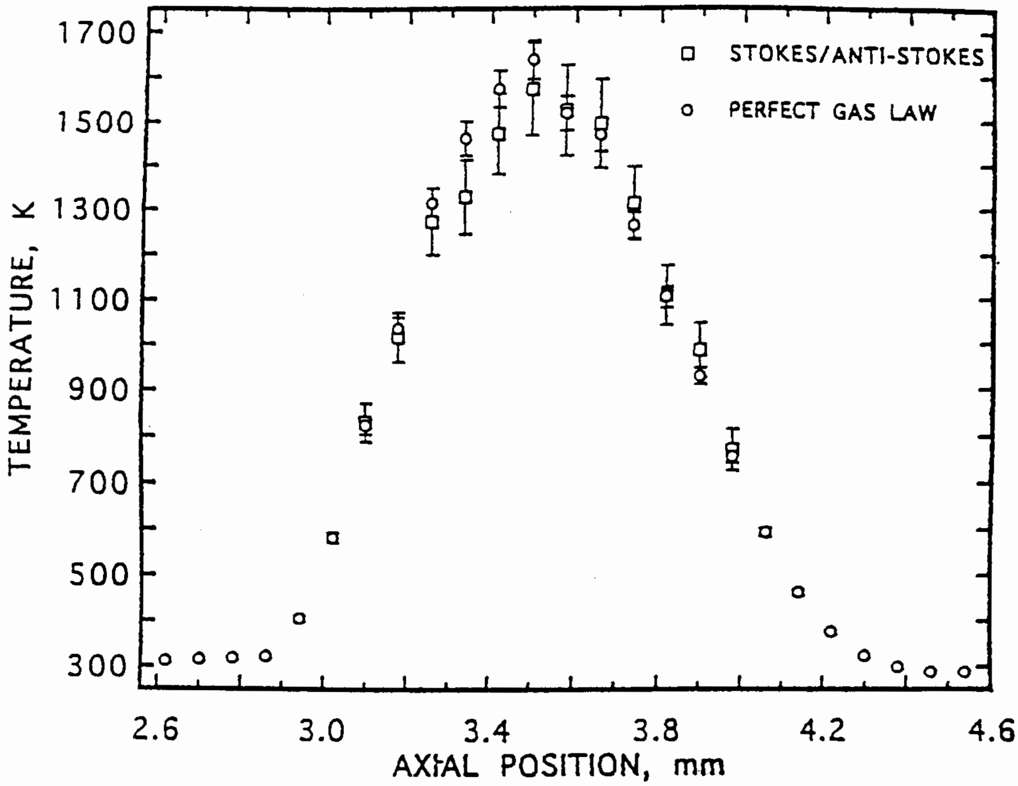

Fig.12 Temperature profiles derived from ideal gas law assumption and Stokes/anti-Stokes ratio for the opposed jet diffusion flame of Fig.10.

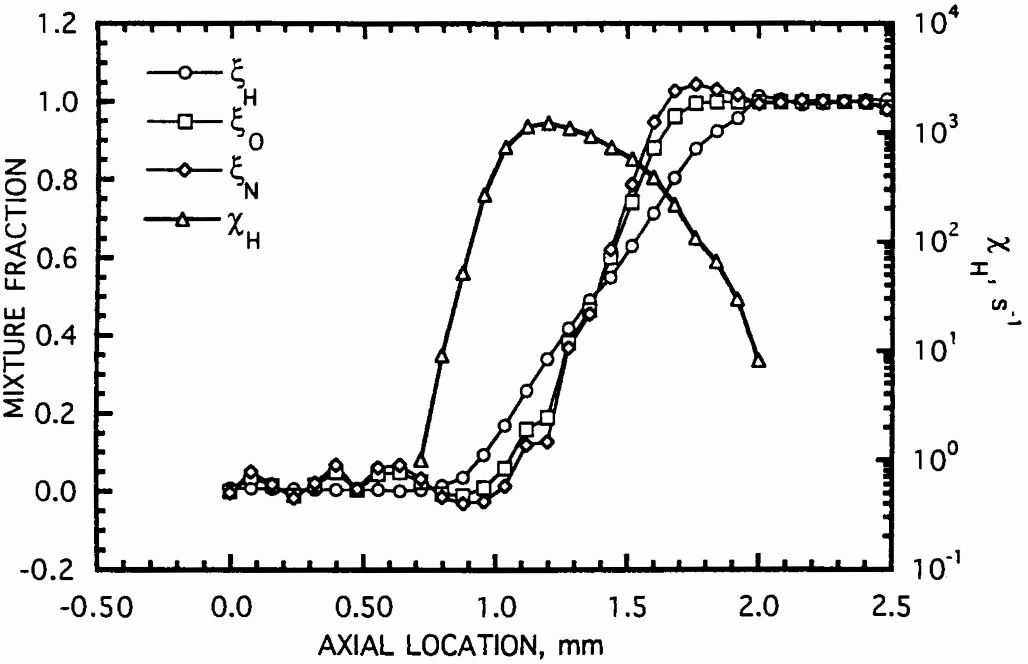

Fig.13 Mixture fraction and scalar dissipation rate in physical space for the equimolar H_2/N_2 flame of Figs. 7 and 10, a=3830 s^{-1}.

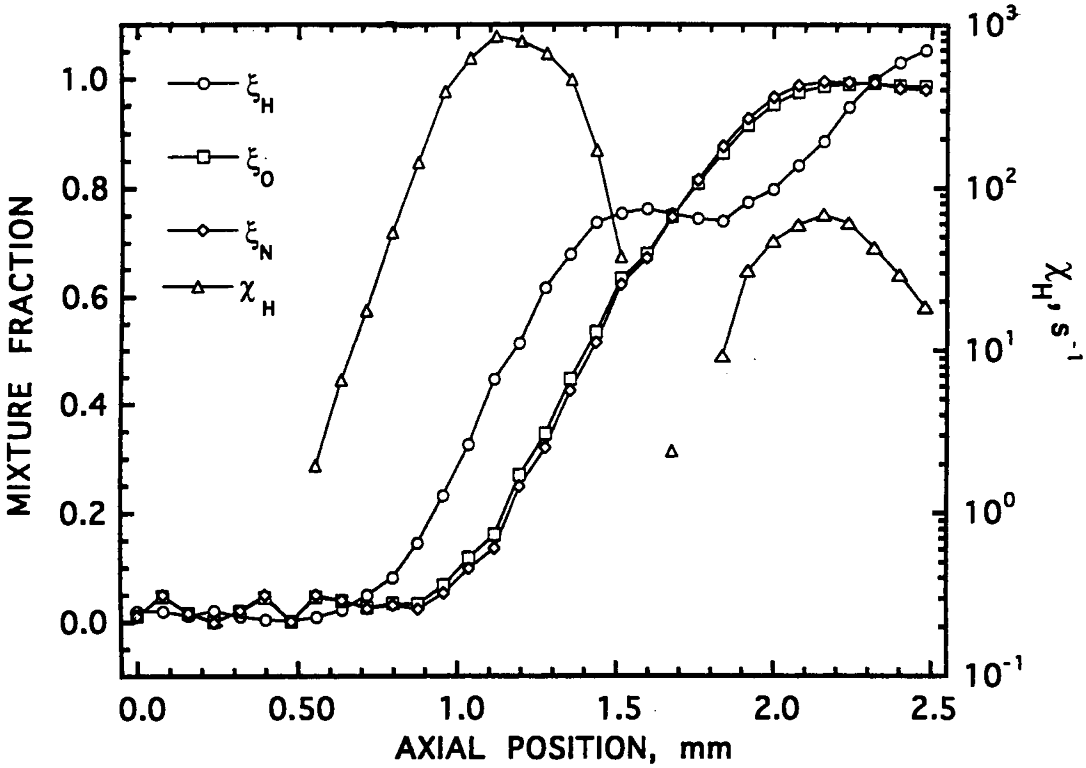

Fig.14 Mixture fraction and scalar dissipation rate in physical space: X_{H_2}=0.21, X_{N_2}=0.79, a=1050 s^{-1}.

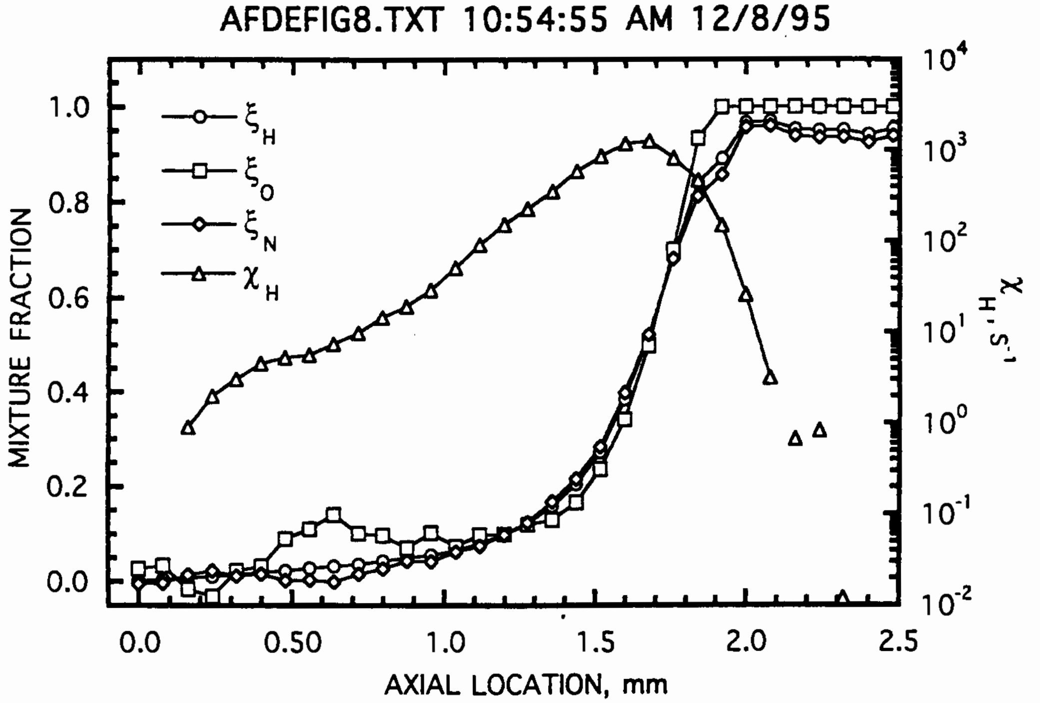

Fig.15 Mixture fraction and scalar dissipation rate in physical space: $X_{H_2}=1$, $X_{N_2}=0$, $a=1240$ s^{-1}.

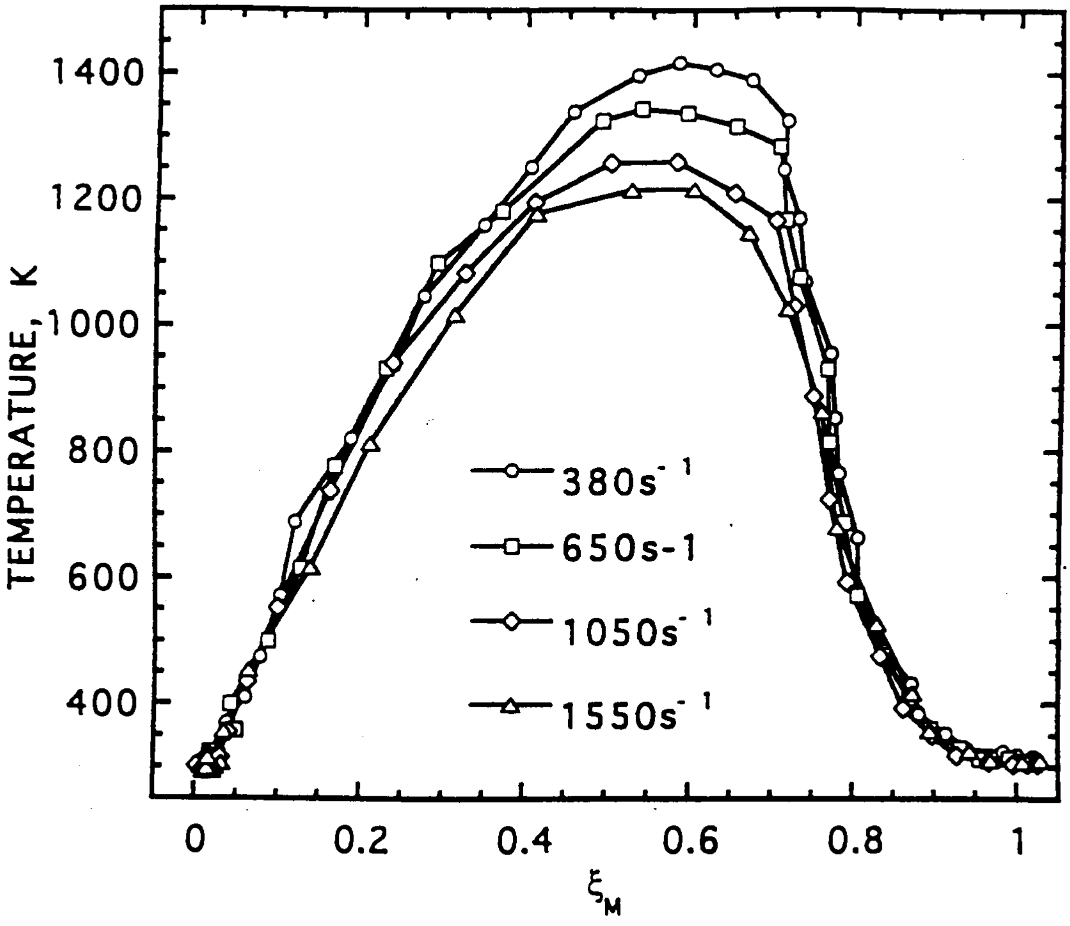

Fig.16 Temperature as a function of mean mixture fraction for four flames at different strain rates: X_{H_2}=0.21, X_{N_2}=0.79.

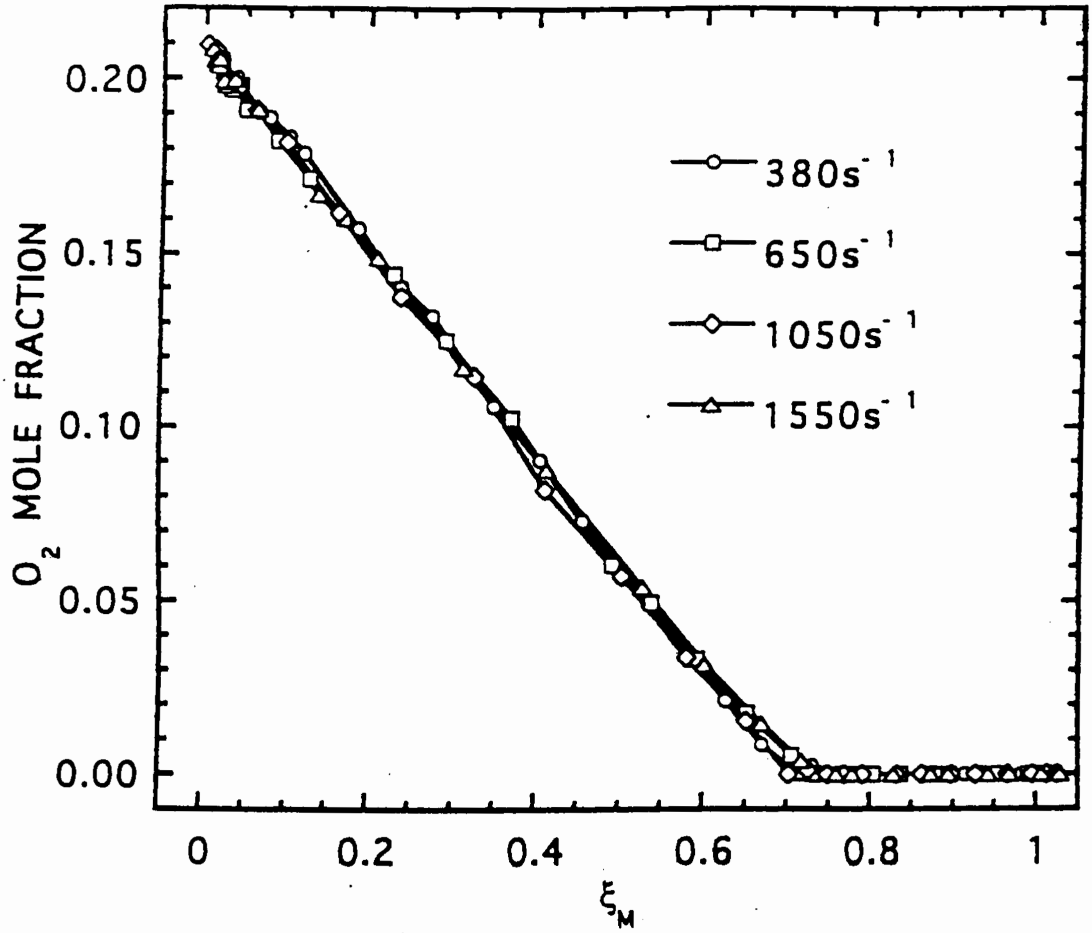

Fig.17 O_2 mole fraction as a function of mean mixture fraction for four flames at different strain rates: X_{H_2}=0.21, X_{N_2}=0.79.

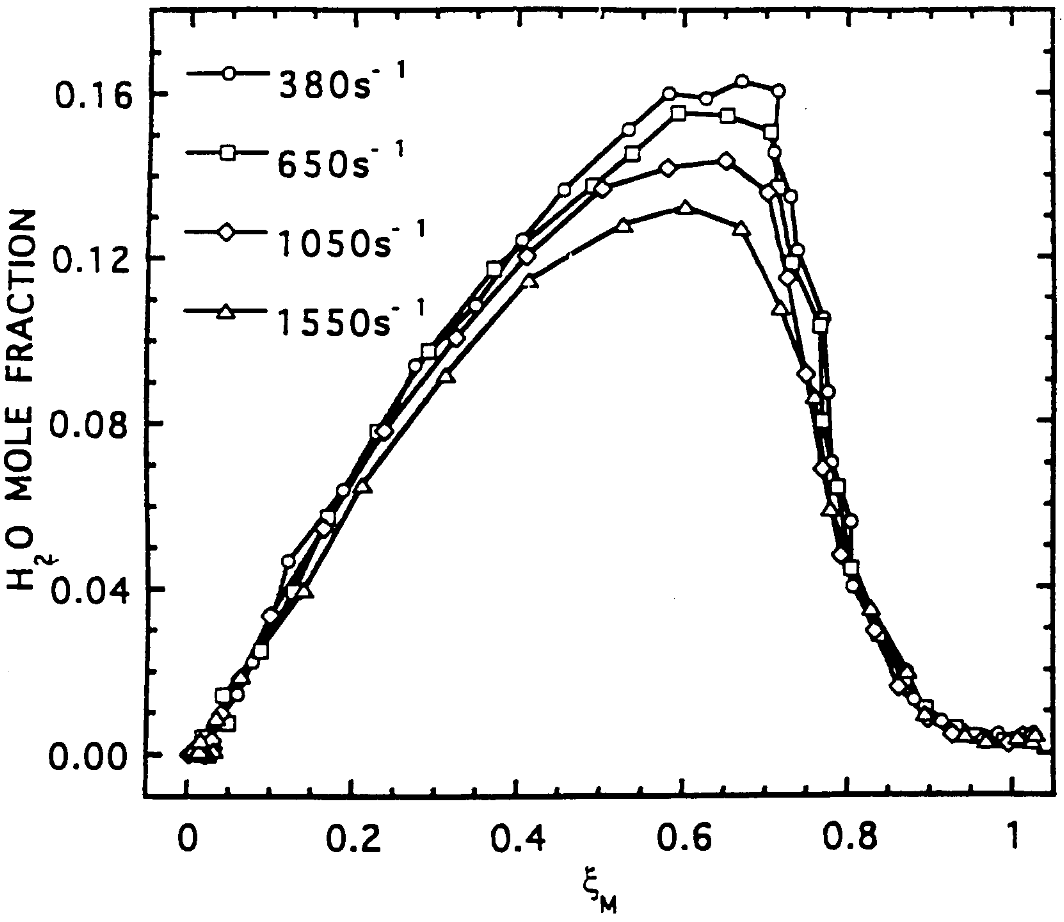

Fig.18 H_2O mole fraction as a function of mean mixture fraction for four flames at different strain rates: X_{H_2}=0.21, X_{N_2}=0.79.

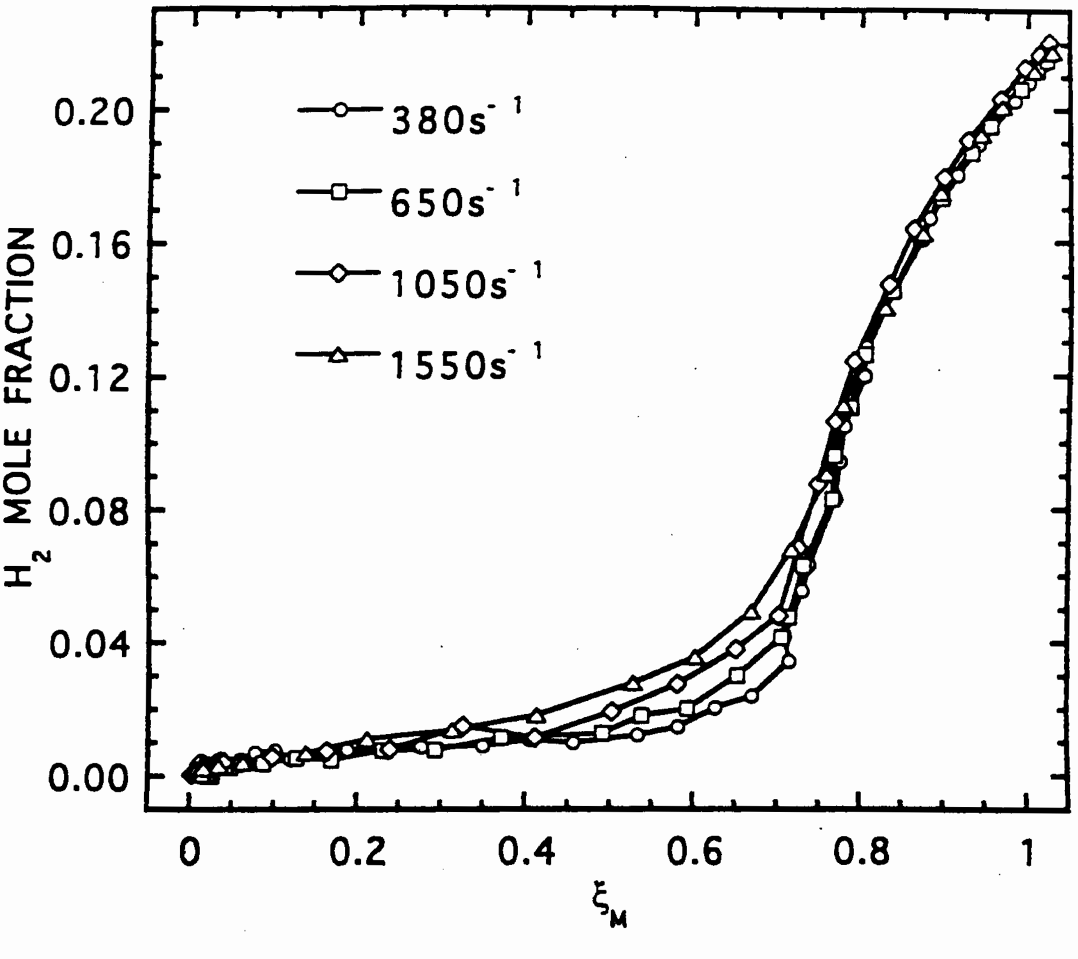

Fig.19 H_2 mole fraction as a function of mean mixture fraction for four flames at different strain rates: X_{H2}=0.21, X_{N2}=0.79.

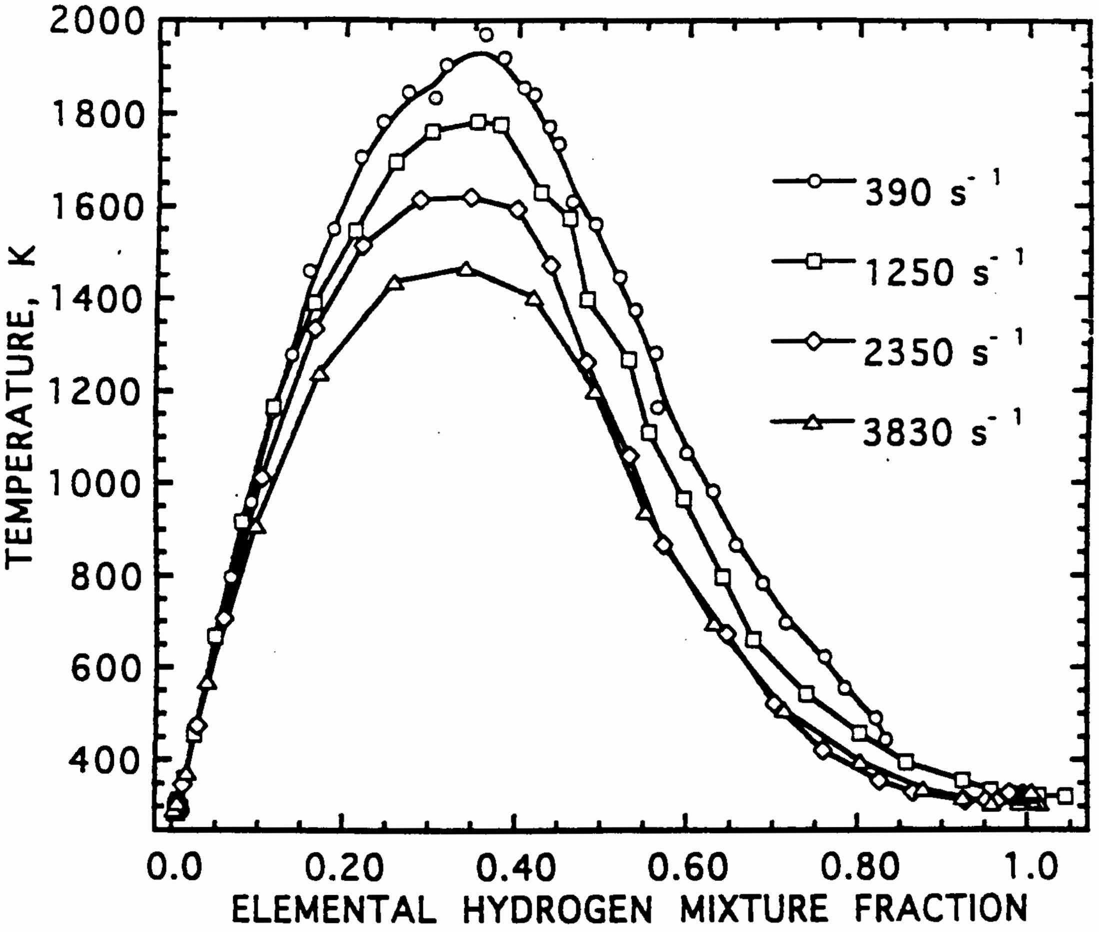

Fig.20 Temperature as a function of hydrogen mixture fraction for four flames at different strain rates: X_{H_2}=0.5, X_{N_2}=0.5.

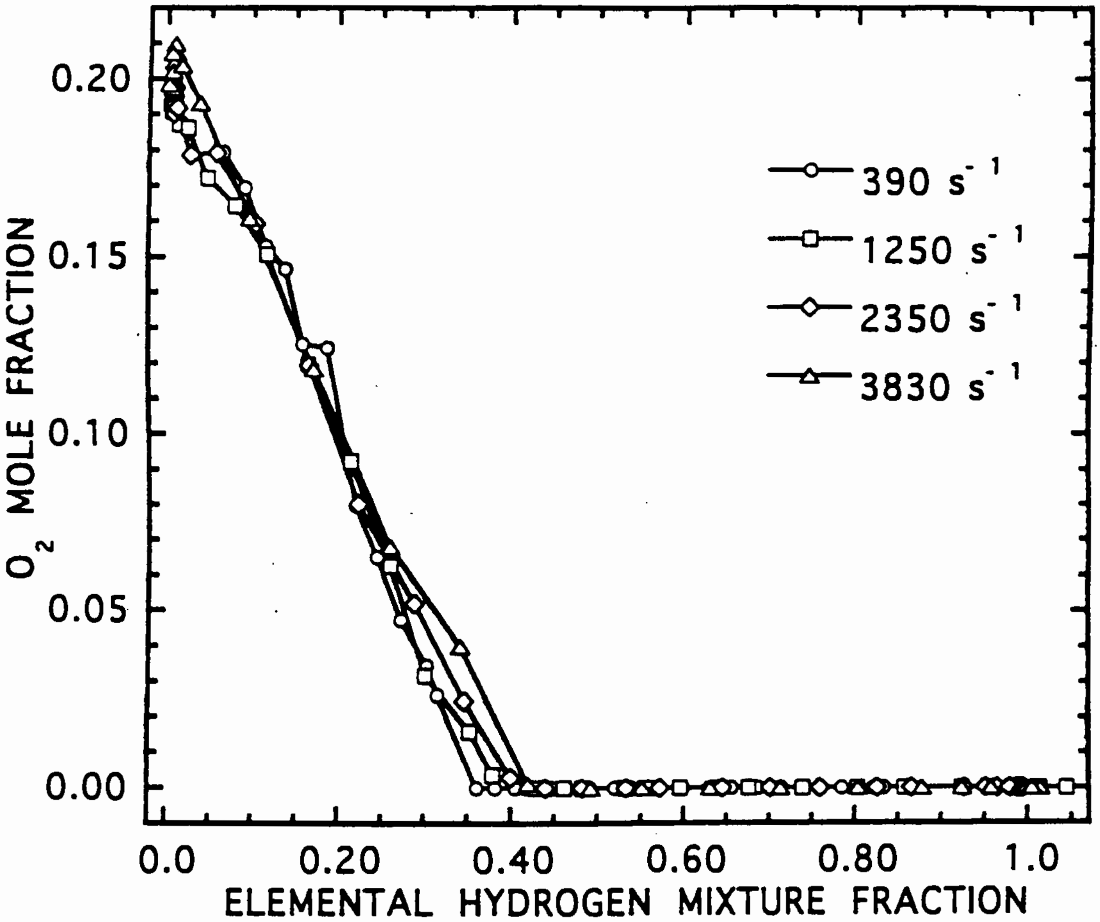

Fig.21 O_2 mole fraction as a function of hydrogen mixture fraction for four flames at different strain rates: X_{H_2}=0.5, X_{N_2}=0.5.

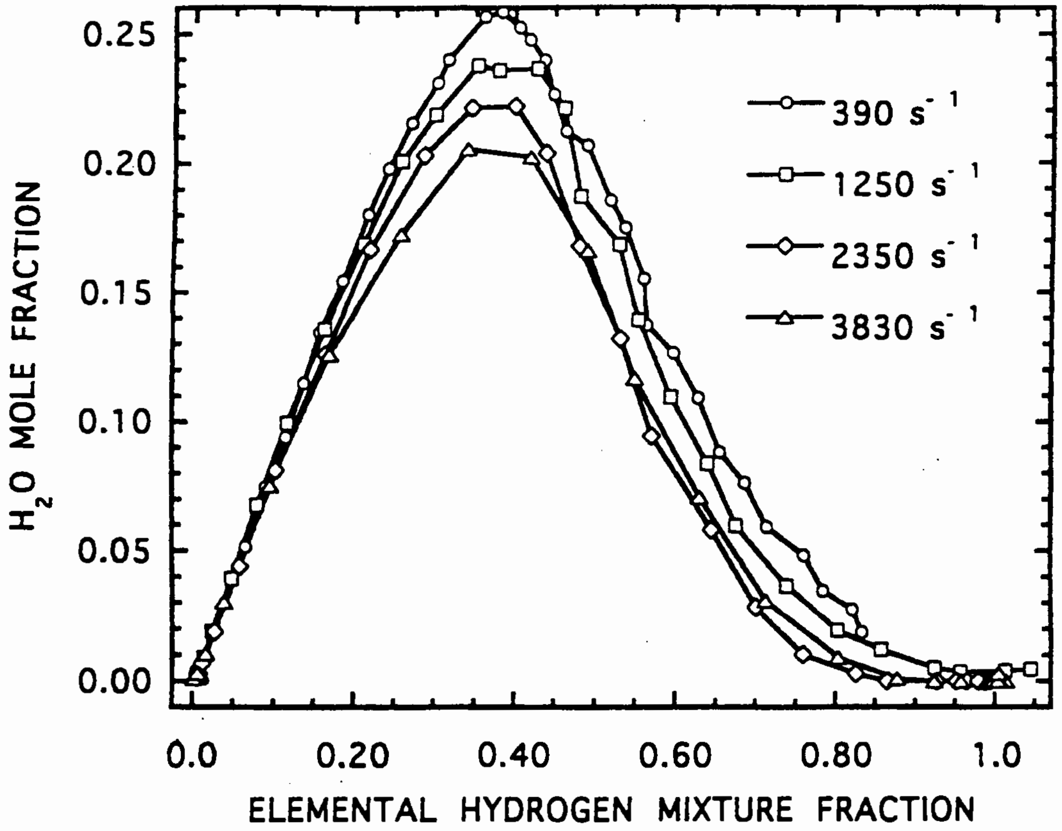

Fig.22 H_2O mole fraction as a function of hydrogen mixture fraction for four flames at different strain rates: X_{H_2}=0.5, X_{N_2}=0.5.

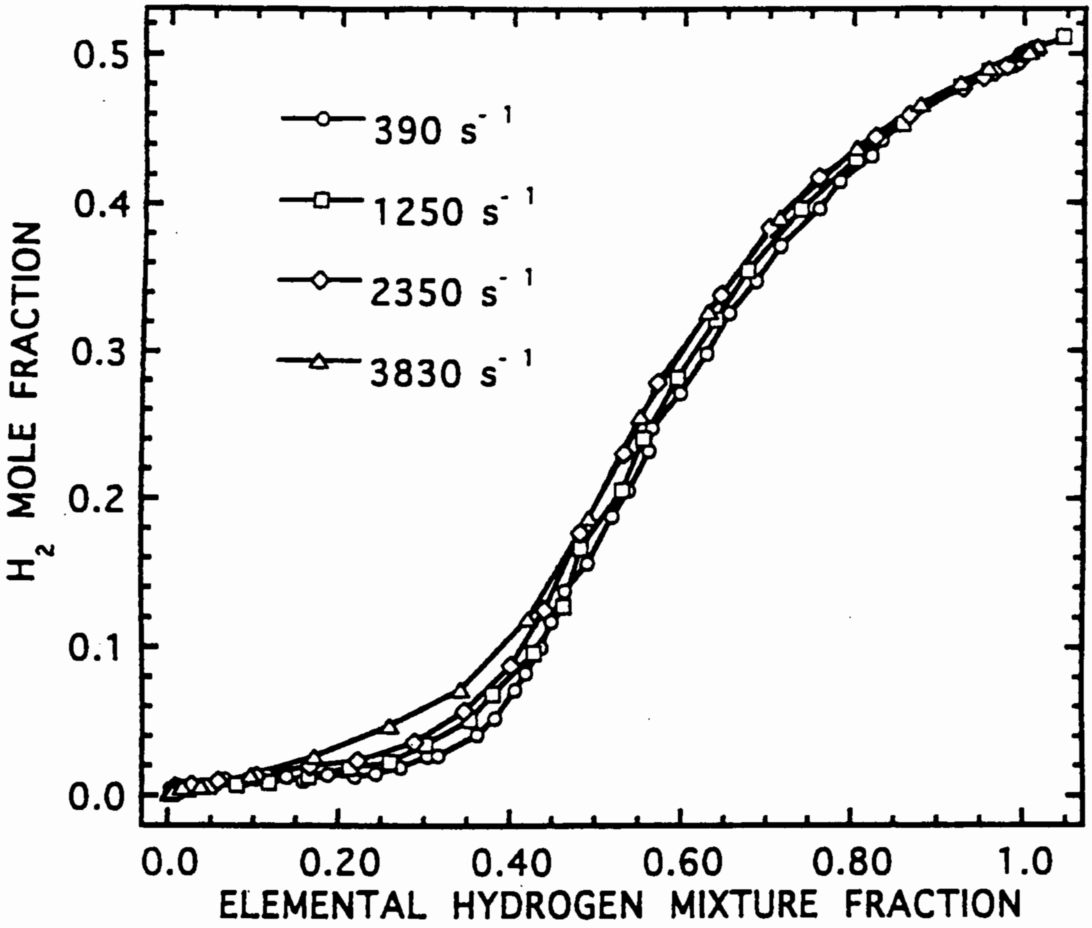

Fig.23 H_2 mole fraction as a function of hydrogen mixture fraction for four flames at different strain rates: X_{H_2}=0.5, X_{N_2}=0.5.

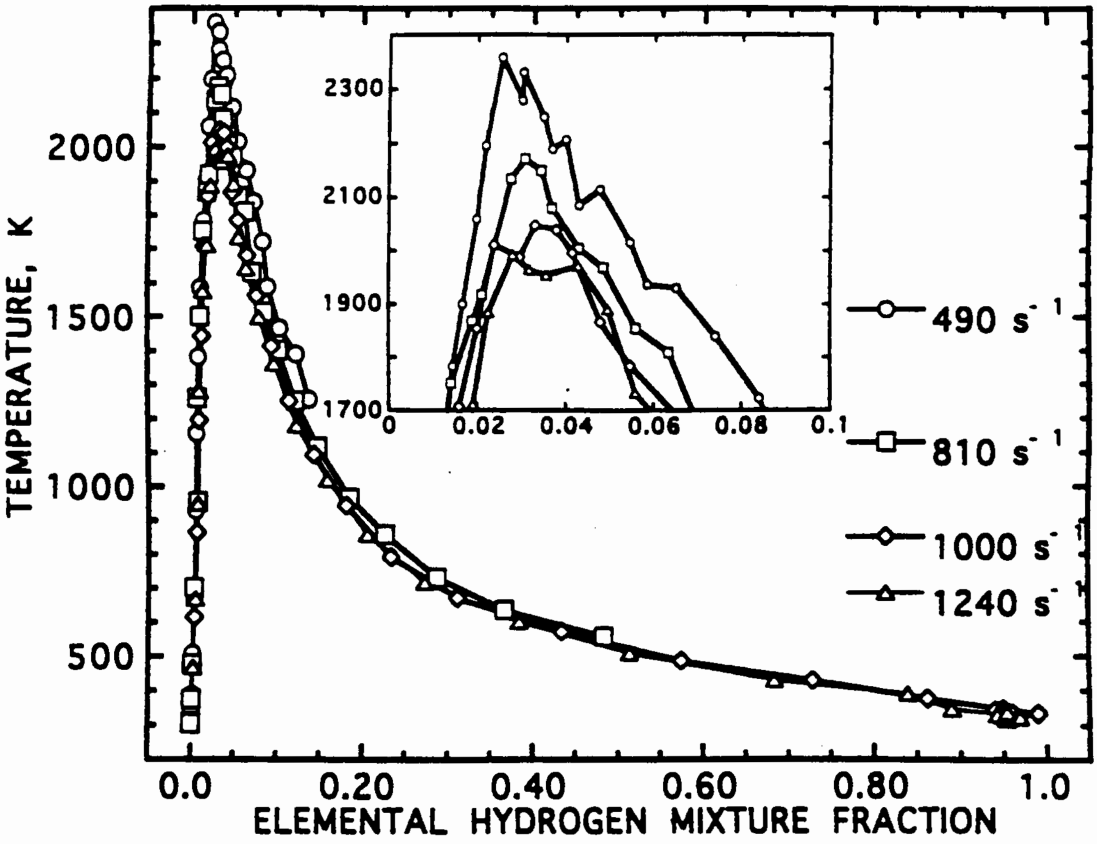

Fig.24 Temperature as a function of hydrogen mixture fraction for four flames at different strain rates: X_{H_2}=1.0, X_{N_2}=0.0.

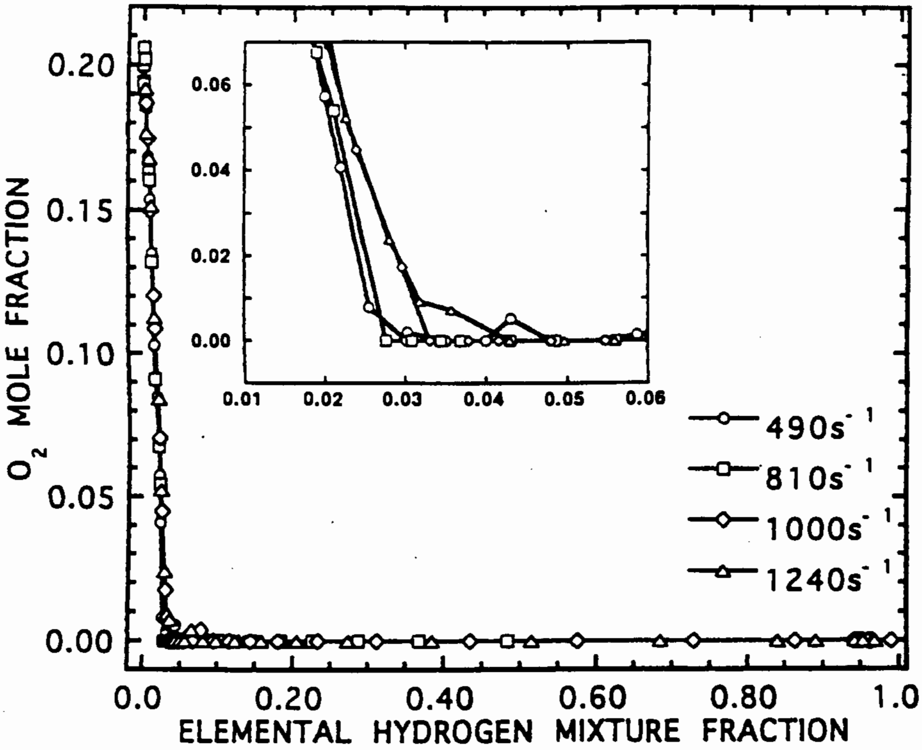

Fig.25 O_2 mole fraction as a function of hydrogen mixture fraction for four flames at different strain rates: X_{H_2}=1.0, X_{N_2}=0.0.

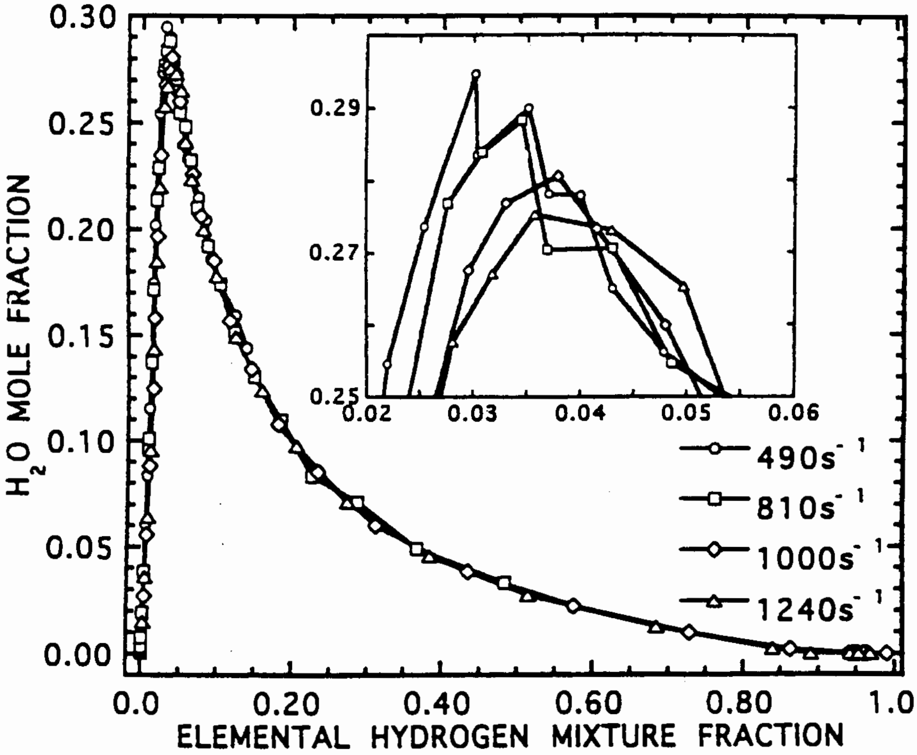

Fig.26 H_2O mole fraction as a function of hydrogen mixture fraction for four flames at different strain rates: X_{H_2}=1.0, X_{N_2}=0.0.

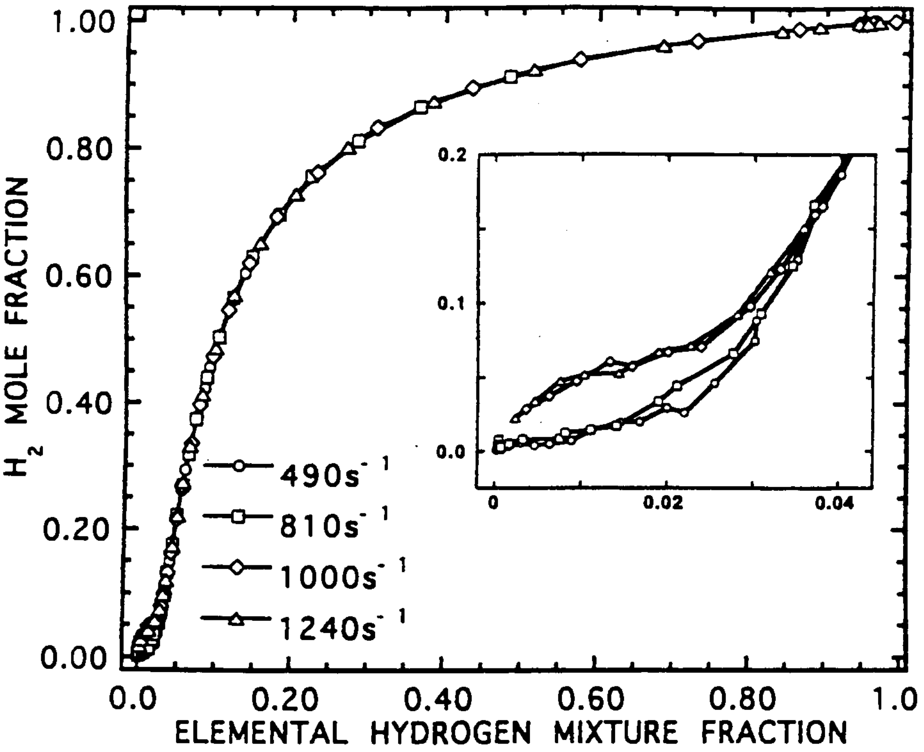

Fig.27 H_2 mole fraction as a function of hydrogen mixture fraction for four flames at different strain rates: X_{H_2}=1.0, X_{N_2}=0.0.

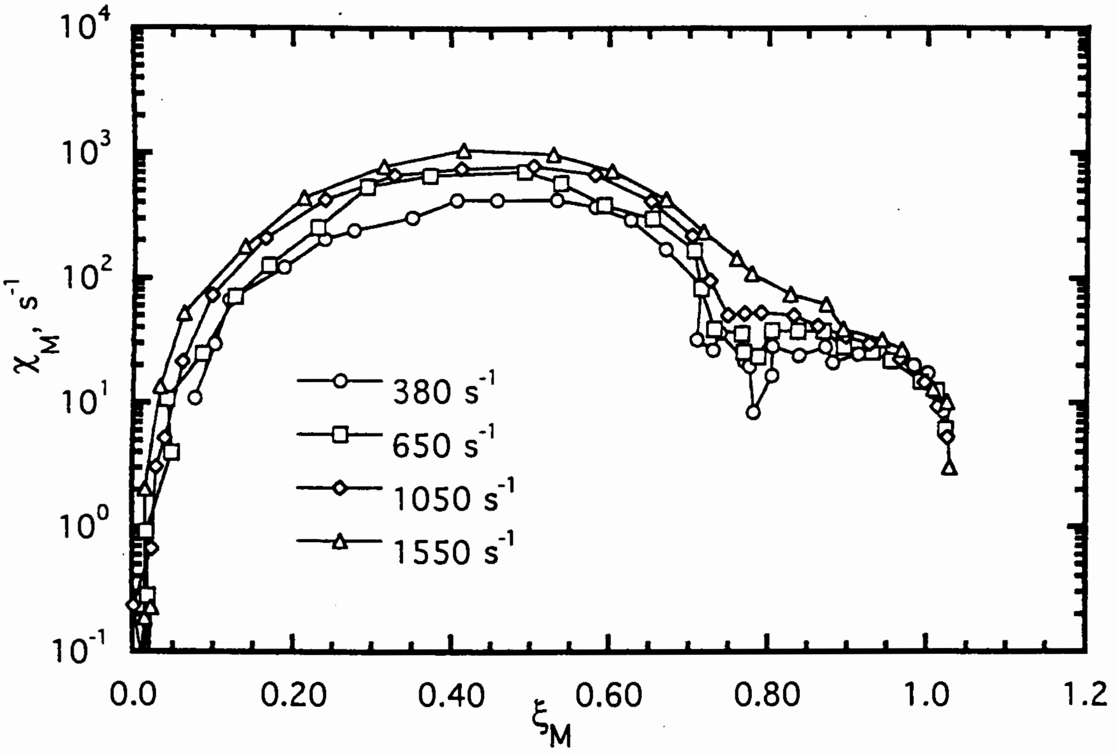

Fig.28 Scalar dissipation rate, based on mean mixture fraction as a function of mean mixture fraction for four flames at different strain rates: X_{H_2}=0.21, X_{N_2}=0.79.

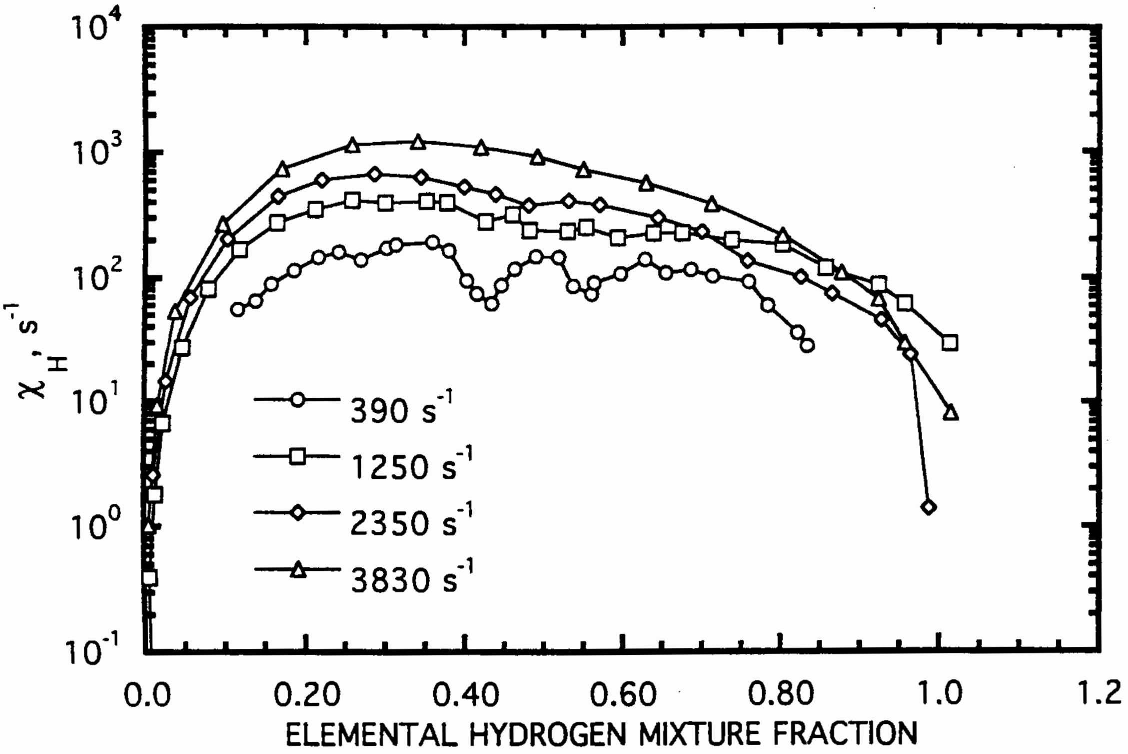

Fig.29 Scalar dissipation rate as a function of hydrogen mixture fraction for four flames at different strain rates: X_{H_2}=0.5, X_{N_2}=0.5.

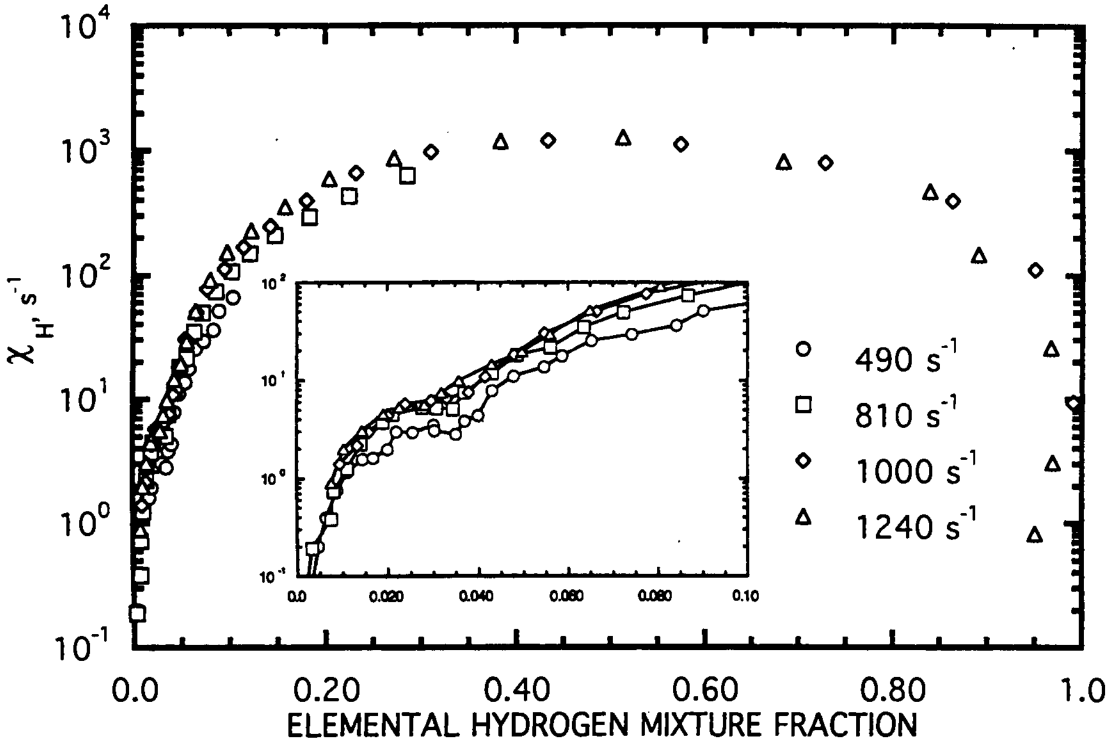

Fig.30 Scalar dissipation rate as a function of hydrogen mixture fraction for four flames at different strain rates: X_{H_2}=1.0, X_{N_2}=0.0.

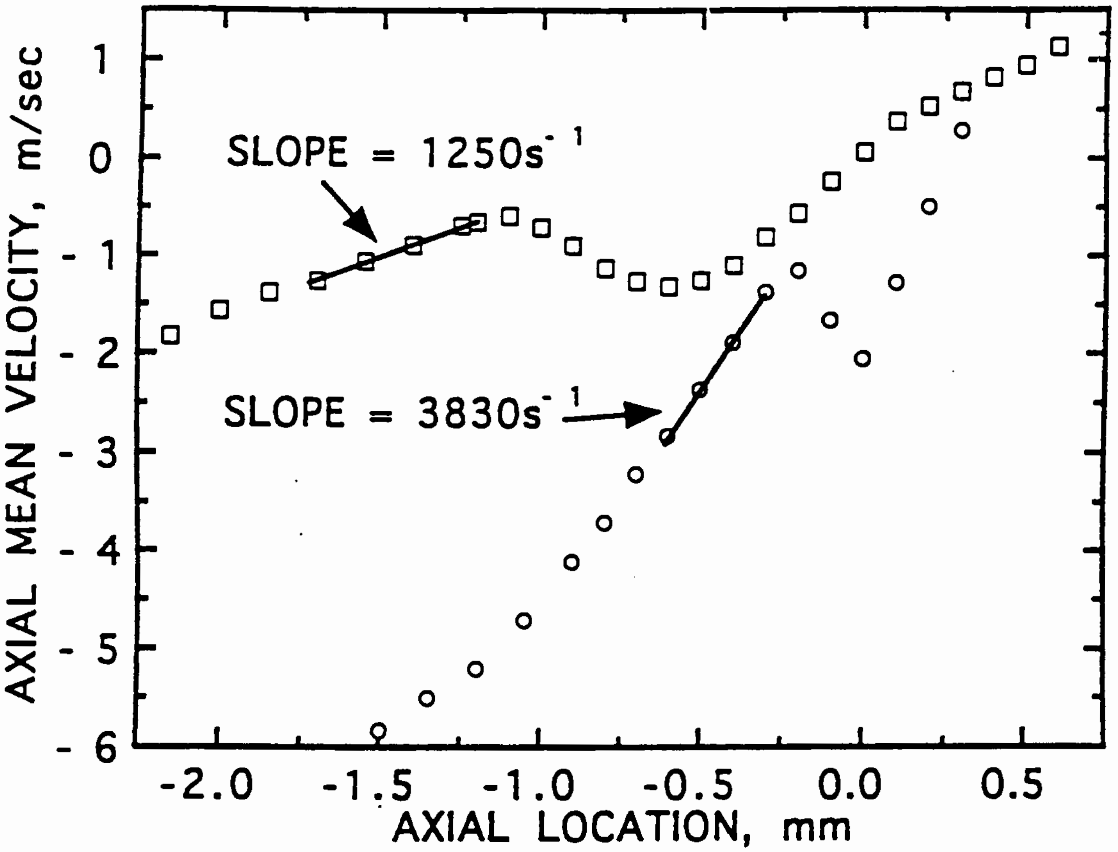

Fig.31 Axial velocity profiles along center line for flames of Fig.9: X_{H_2}=0.5, X_{N_2}=0.5.

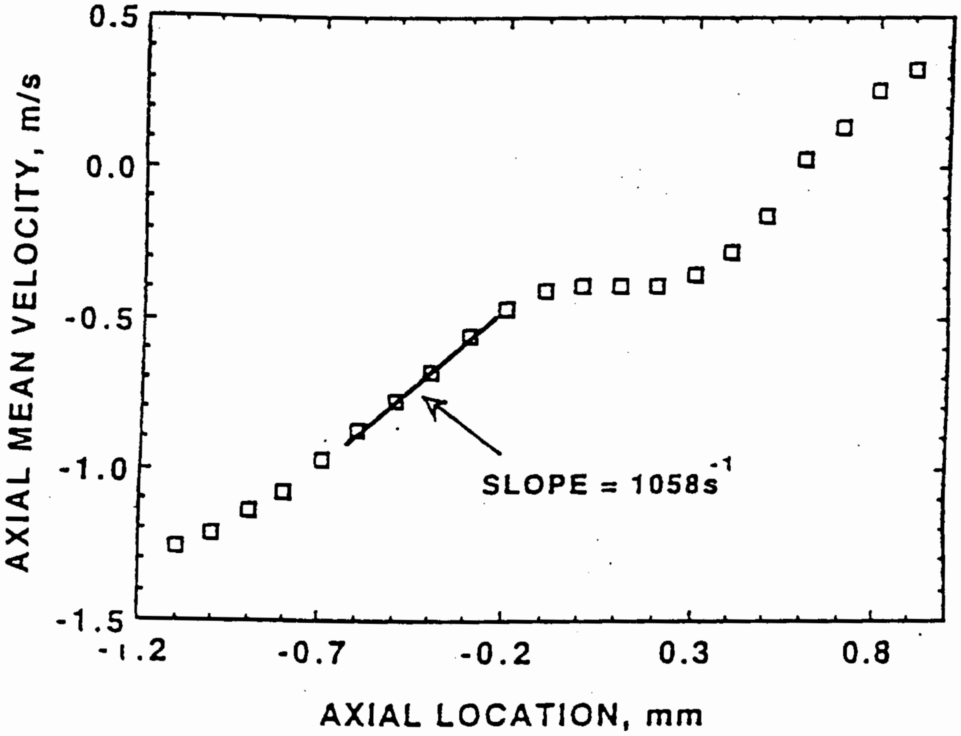

Fig.32 Axial velocity profile along center for flame of Fig.14: X_{H_2}=0.21, X_{N_2}=0.79.

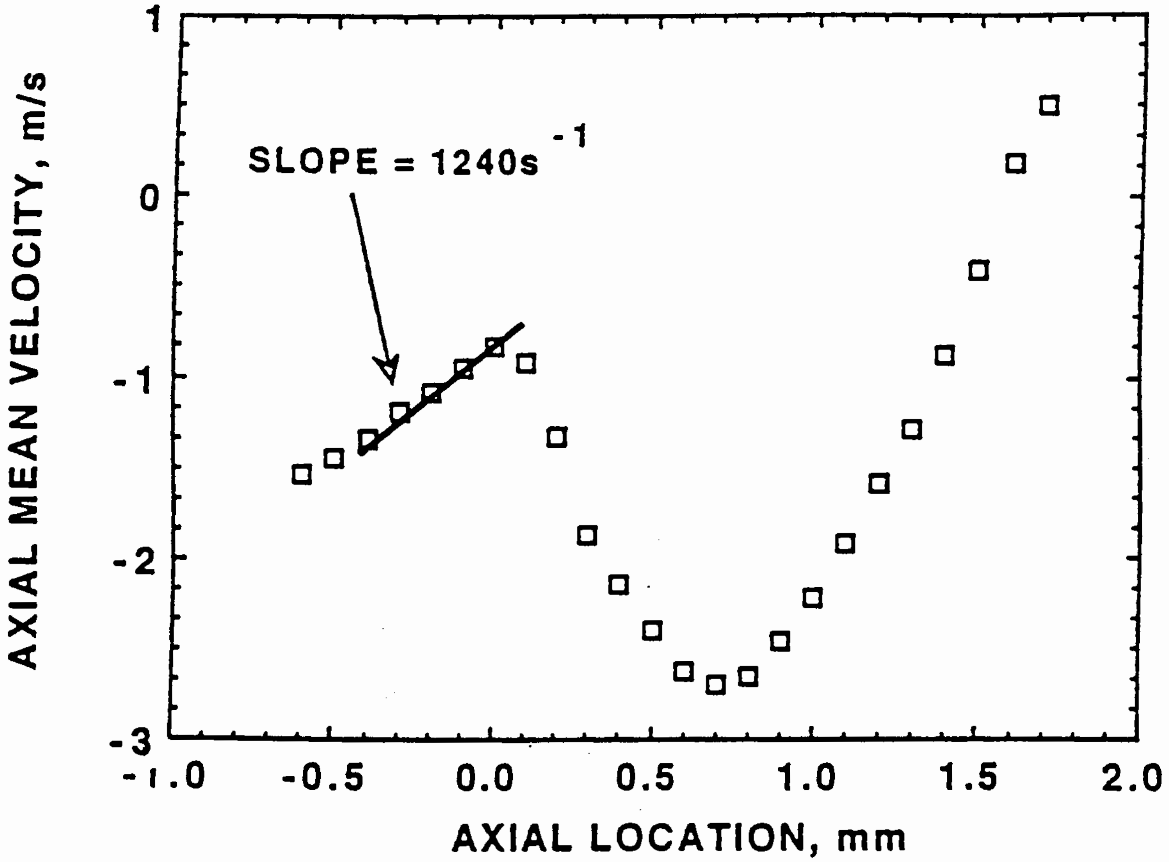

Fig.33 Axial velocity profile along center for flame of Fig.15: X_{H_2}=1.0, X_{N_2}=0.0.

CHAPTER-V

CONCLUSIONS

Optical diagnostic systems applied to combustion studies face many challenges. Highly turbulent fluid motion requires high temporal and spatial resolution systems that can operate accurately. Above all, the physical environment that optical systems are placed in is usually abrasive and unkind to sensitive measuring devices. The present thesis offers a unique way of applying Raman spectroscopy to investigate laminar flame structures. An unintensified liquid nitrogen cooled charge-coupled device (CCD), along with a fast gating ferro-electric liquid crystal light valve (FLC) combination achieves high signal to noise ratio and high precision (2% uncertainty). Comparison with a parallel system that uses an intensified CCD instead of a liquid nitrogen cooled CCD coupled with an FLC shows ~40% reduction of signal-to-noise ratio [Wehrmeyer, Yeralan and Tecu 1995a]. However, there are combustion systems with high flame luminosity and/or high turbulent fluctuations that require faster gating than what is possible with an FLC (~40 μs). Under these conditions the experimental system favors an intensified CCD over the unintensified counterpart.

Another important aspect of the experimental arrangement is the unique co-axial placement of the opposed jet burner and the laser beam path. This allows a linewise investigation of the flame front located at the center of a disk-shaped hydrogen diffusion flame. The 90 degree angle collection optics serves well to image the laser pierced section of the flame. Raman imaging of the flame on a CCD allows a one-dimensional investigation of the flame from a single acquisition which is more convenient compared to multiple pointwise measurements that together would comprise a similar result [Cheng, Wehrmeyer and Pitz 1992; Barlow and Carter 1994].

The same experimental set-up demonstrated the possibility of obtaining temperature information using the Stokes/anti-Stokes signal ratio [Wehrmeyer, Yeralan and Tecu 1995b]. The comparison of two temperature profiles, one obtained by utilizing the ideal gas law and the other by utilizing Stokes/anti-Stokes ratio, resulted in good agreement. The minor disagreement between the two temperature profiles is located on the air side of the peak temperature location where minor species such as OH make relatively significant contribution to the total number density. This contribution is ignored by the temperature measurement method assuming that the total number density is comprised of major species contributions and they are in ideal gas state. Single shot temperature measurement capability of the experimental system has also been investigated [Wehrmeyer, Yeralan and Tecu 1995b]. Although the uncertainty increased from 6% to 19% for single shot, compared to the integrated 200 shots, Stokes/anti-Stokes temperature measurements, single shot temperature measurements are valuable in turbulent combustion systems with varying pressure.

The experimental uncertainty can be improved by higher signal intensity. This is achievable by use of a higher power laser. Since the Raman cross-section of molecules increase by fourth power of the incident radiation frequency, a lower wavelength laser would increase the signal strength as well. It should be noted that one must take into consideration the CCD and FLC spectral characteristics since the efficiency of the CCD and/or FLC may decrease if longer wavelength laser radiation is chosen. There may be a number of improvements to FLC. The replacement of the sheet polarizers with more efficient crystal polarizers would improve the signal to noise ratio. The thickness of the FLC may be optimized to the wavelength region of interest. Finally, a backside-illuminated CCD may be substituted for the present CCD to improve the efficiency of the system [Plath, Meier and Stricker 1992].

There is much information gained from hydrogen diluted with nitrogen versus air opposed jet diffusion flame studies. Temperature and major species mole fraction profiles are gathered in these flames via linewise Raman imaging. The experimental uncertainty of 2% and spatial resolution of 160 μm are accomplished over a 200 shot integration. The spatial resolution of 160 μm results from a superpixel size of 80 μm, 500 μm beam waist contribution of 60 μm, and optical aberrations of 20 μm.

The experimentally investigated flame conditions include three different fuel dilutions. Flames with highly diluted fuel jets (21% H_2+79% N_2) versus air are studied over strain rates ranging from 380 s^{-1} to 1550 s^{-1}. The flames of equimolar dilution of the fuel jet are studied over strain rates 390 s^{-1} to 3830 s^{-1}. Flames that correspond to undiluted fuel stream are studied over strain rates from 490 s^{-1} to 1240 s^{-1}.

Temperature and major species mole fraction profiles reveal important characteristics of opposed jet diffusion flames. An increase in strain rate is accompanied by a decrease in peak temperature and water vapor mole fraction values. The thinning of the water vapor mole fraction profile and temperature profile with increasing strain rate is demonstrated. The greater leakage of the hydrogen and oxygen through the flame zone with increasing strain rate demonstrates that as the characteristic fluid mechanical time is reduced the diffusion process and chemical kinetics are less complete. It is illustrated that as the strain rate is increased, the gradients of hydrogen and oxygen mole fraction profiles are increased.

Generally temperature values of the flames matched well with numerical predictions [Dixon-Lewis and Missaghi 1988]. The only discrepancy between the numerically and experimentally suggested temperatures occurred in the flames burning undiluted hydrogen. The peak temperature values of these flames are 100 K to 300 K higher compared to a numerical investigation of Gutheil and her co-worker [Gutheil and Williams 1991]. The same flame temperatures compare better with another set of numerical data obtained by Dixon-Lewis and Missaghi [1988]. The experimentally determined peak temperature values of pure fuel burning flames are 50 K to 100 K higher then what is suggested by these authors. Some of the possible reasons for these discrepancies include experimental uncertainties and thermophoretic effect causing erroneous velocity measurements. Flame curvature may also increase the temperature of the center of the flame in these opposed jet H_2-air flames. This increase in temperature is mainly attributed to the radiation effects where the center location would have a higher temperature surrounding it, compared to a one dimensional flame, due to the flame curvature. Thus less radiation heat loss would result in a higher temperature at the center. This aspect is investigated and found to be insignificant for the flowrates that are used in this dissertation. Further details are included in Appendix C.

After major species mole fraction profiles in physical space are obtained, mixture fraction values are calculated. Differences between the elemental mixture fraction profiles of hydrogen, oxygen and nitrogen demonstrate significant differential diffusion effects. The numerically predicted characteristic "S-shape" of the hydrogen mixture fraction profile when the fuel is diluted by 79% by N_2, is experimentally demonstrated [Dixon-Lewis and Missaghi 1988]. Another differential diffusion characteristic that is experimentally investigated is the "overshoots" of nitrogen and oxygen mixture fraction profiles of opposed jet flames with equimolar dilution of hydrogen. These trends of differential diffusion effects have been numerically predicted [Dixon-Lewis and Missaghi 1988] but have never been experimentally demonstrated until now.

Scalar dissipation rate profiles of the opposed jet flames are calculated. Multi-component diffusion coefficients of the scalar dissipation rate calculations are gathered from CHEMKIN chemical kinetics computer model. The diffusion coefficients are corrected for the correct gas mixture composition and temperature at the flame location. This is accomplished by first calculating the individual species binary diffusion coefficients at various temperatures and then calculating Fick's law of multi-component diffusion coefficient for elemental hydrogen. It is observed that as the strain rate increased, scalar dissipation rate peak values increased. For example as strain rate increased from 390 s^{-1} to 3830 s^{-1}, scalar dissipation rate increased from 200 s^{-1} to 1240 s^{-1} for equimolar concentration of H_2/N_2 fuel jet flames. For the two lower strain rate cases of Fig.30 (undiluted fuel jet cases), the scalar dissipation profiles include relative minima around the stoichiometric location that is numerically predicted to happen at strain rates that are lower than the examined strain rates [Gutheil and Williams 1990].

The present thesis is valuable in the areas of optical diagnostics of combustion environments and opposed jet diffusion flame studies. The established experimental arrangement is capable of linewise Raman imaging with high precision and dynamic range. High dynamic range (16383 counts) of the liquid nitrogen cooled CCD allows long integration of Raman images directly onto the CCD resulting in high signal-to-noise ratio (2% uncertainty). Single shot capability of the system is also demonstrated by single shot Stokes/anti-Stokes temperature measurements of hydrogen diffusion flames. In opposed jet flame experiments, fuel stream composition along with axial strain rate are varied to investigate different aspects of hydrogen combustion. The much needed flamelet library of mixture fraction and scalar dissipation rate profiles as functions of strain rate are obtained.

Further improvements to the investigation involve radical concentration measurements, especially OH. Measurements of short lived, intermediate species such as OH are necessary for complete understanding of hydrogen combustion chemistry. Another important side of turbulent combustion is the vortex interactions. These effects can be simulated by reproducible perturbations such as acoustically caused vortices. This would lead to further investigation of time varying aspect of combustion zone.

APPENDIX-A

THERMOCOUPLE MEASUREMENTS

Temperature measurements of the calibration flames are extremely vital for an accurate calibration of the experimental system. Temperature measurements need to be corrected for radiation effects since high temperatures are encountered in these flames. Radiation correction of thermocouple temperature measurements is accomplished by using two different thermocouples [Nichols 1900]. Different bead diameters of the Pt30%Rh vs Pt6%Rh thermocouples allow some estimate of the radiation effects. The two nominal bead diameters that are used in this dissertation are 0.011 and 0.017 inches. A graph of bead diameter versus temperature for a rich H_2-air flame (equivalence ratio=5) results in a linear relation as shown in Fig.34. As the thermocouple bead size gets smaller, the higher, more accurate, temperature values are indicated by the thermocouple. Simply extrapolating to zero diameter bead size, one can correct for radiation effects. The accuracy of the technique increases with increasing number of temperature readings by several diameter thermocouple beads.

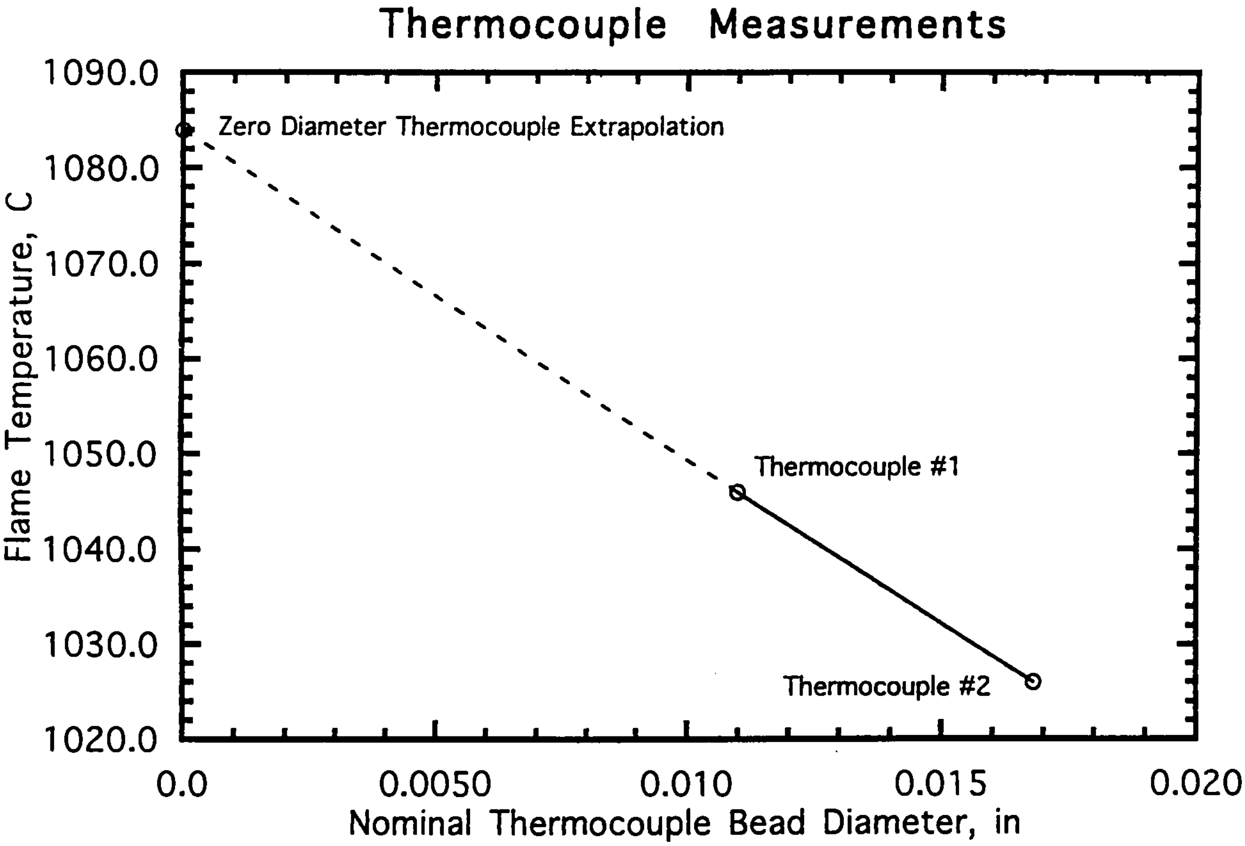

Fig.34 Radiation corrected temperature measurements.

APPENDIX-B

WORKING EQUATIONS

The intensity of Raman signal depends on the molecular dipole moments of the species under examination. However, these dipole moment values are not available for most of the species, they can be approximated by using Placzek's polarizability theory [Placzek 1934]. It should be realized that as molecular structure becomes more complicated, evaluation of the molecular constants gets to be immensely difficult. One can derive the following equation which describes the intensity of a single Stokes Q-branch transition (Δv=+1, ΔJ=0):

$$I(v,J)\alpha\frac{(2J+1)g_i e^{(\frac{-Ej}{kT})} e^{(\frac{-Ev}{kT})}(v+1)(v_o-v_{nm})^4}{Q_{rot}Q_{vib}} \qquad \text{(B-1)}$$

In the above equation, v represents the vibrational quantum number, J represents the rotational quantum number, g_i is the spin degeneracy, Q_{rot} and Q_{vib} are the rotational and vibrational partition functions respectively.

The intensity of the Stokes Raman Q-branch signal when it is summed over all the rotational and vibrational levels is:

$$I_{Stokes}\alpha N_{Total}(v_o-v_v)^4 Q_{vib} \qquad \text{(B-2)}$$

where N_{Total} is the total number density of the species. The integrated intensity of the anti-Stokes Q-branch (Δv=-1, ΔJ=0) is:

$$I_{anti-Stokes} \alpha N_{Total}(\nu_o + \nu_v)^4 (Q_{vib} - 1) \qquad \text{(B-3)}$$

The above equations represent the complexity of scattering phenomena. These equations can be greatly simplified for the engineering applications. The Raman photons are collected at 90 degree angle to the laser path way in the experiments for this dissertation. The collected Raman energy in this configuration can be reduced to the following form [Lapp et al. 1973]:

$$E_R = E_L L \Omega n \sigma_{zz} f(T) \qquad \text{(B-4)}$$

where E_R is the energy of the total Raman photons, E_L is the laser energy per-pulse, L is the length of the control volume, n is the number density of the scattering molecule, Ω is the optical efficiency, σ is the vibrational Raman cross section of the scattering molecule and the f(T) accounts for the temperature dependence of the spectrometer slit function. When the Raman signal is collected by a photomultiplier tube (PMT) or a charge-coupled detector (CCD) in conjunction with some optical lenses and a spectrometer, the gathered signal intensity can be calculated by:

$$N = n \frac{\eta (QE) L \Omega \sigma_{zz} E_L}{h\nu_s} f(T) \qquad \text{(B-5)}$$

where all the symbols are the same as Eq. B-4 and in addition η is the optical efficiency, QE is the quantum efficiency of the detection system, and $h\nu_S$ factor in the denominator converts the energy into number of Raman photons.

It should be noted that the ratio of the intensities of Stokes and anti-Stokes Raman signals is a sole function of temperature. One can derive at this result by the following:

$$\frac{I_{Stokes}}{I_{anti-Stokes}} = c(\frac{v_{Stokes}}{v_{anti-Stokes}})\frac{Q_{vib}}{(Q_{vib}-1)} \qquad \text{(B-6)}$$

substituting the expression for Q_{vib},

$$Q_{vib} = \frac{1}{1-e^{(\frac{-T_v}{T})}} \qquad \text{(B-7)}$$

results in,

$$\frac{I_{Stokes}}{I_{anti-Stokes}} = c(\frac{v_S}{v_{AS}})^4 e^{(\frac{T_v}{T})} \qquad \text{(B-8)}$$

By manipulating Eq. B-8 one can derive at:

$$T = \frac{T_v}{\ln(\frac{I_{Stokes}}{I_{anti-Stokes}}) + 4\ln(\frac{v_{AS}}{v_S}) - \ln(C)} \qquad \text{(B-9)}$$

where T_V is the characteristic vibrational temperature (3354 K), C is the ratio of the data gathering efficiency of the system for the Stoke vs the anti-Stoke Raman signals. Similarly, v_{AS}, v_S and I_{Stokes}, $I_{anti-Stokes}$ respectively refer to the Stoke and anti-Stoke Raman photons frequency and their intensity. Thus, by using the above equation, measurements of temperature can be obtained with the Raman light scattering.

APPENDIX-C

TRANSVERSE RAMAN DATA

One of the main concerns of opposed jet experiments is the assumption of one dimensionality of the flame. The computer models readily solve the necessary equations with the assumption of one dimensional flame geometry. In the actual experiments there exists a radius of curvature to the flame front especially when the fuel jet is undiluted hydrogen. Although opposed jet measurements are gathered on the centerline of the flame front, one dimensionality of the flames is investigated. Raman measurements of an opposed jet flame are gathered at different off-centerline locations. The resultant opposed jet flame water profiles are displayed in Fig.35. In this figure, traversing in one outward direction from the centerline is arbitrarily chosen to be the positive direction.

The linear relation of Raman signal strength to water molecule's number density is used to investigate one dimensionality of the opposed jet flames. It is evident that if there were indeed a curvature to the flame, then water Raman profiles would shift to lower values with increasing temperature. The centerline water profile would have the lowest values at every axial location compared to the rest of the profiles. The ±0.5 mm off-centerline water Raman signal counts would be consistently lower than ±1.0 and ±1.5 mm off-axis water Raman signal values. This shift in water Raman values would indicate that the flame has a curvature and there exists a temperature gradient caused by this curvature. Furthermore, one would expect to see this temperature gradient to be symmetric about the centerline. Thus the water Raman signal intensities would be very similar for profiles that correspond to locations symmetric about the axis of the opposed jet burner. As the Fig.35, which has equimolar concentrations of hydrogen and nitrogen as the fuel jet, represents there is not an obvious shift in these water profiles. It is also evident that there is no hierarchy in the profiles that suggest similar water Raman signal values for locations that are symmetric about the centerline. The same investigation is carried out for a flame which has undiluted hydrogen as the fuel jet. The water Raman profiles for this flame is displayed in Fig.36. Once again there is no hierarchy in the water signal strength and there is no symmetry of the profiles about the centerline. Thus it is concluded that the oppose jet flames that are investigated in this dissertation are indeed one dimensional.

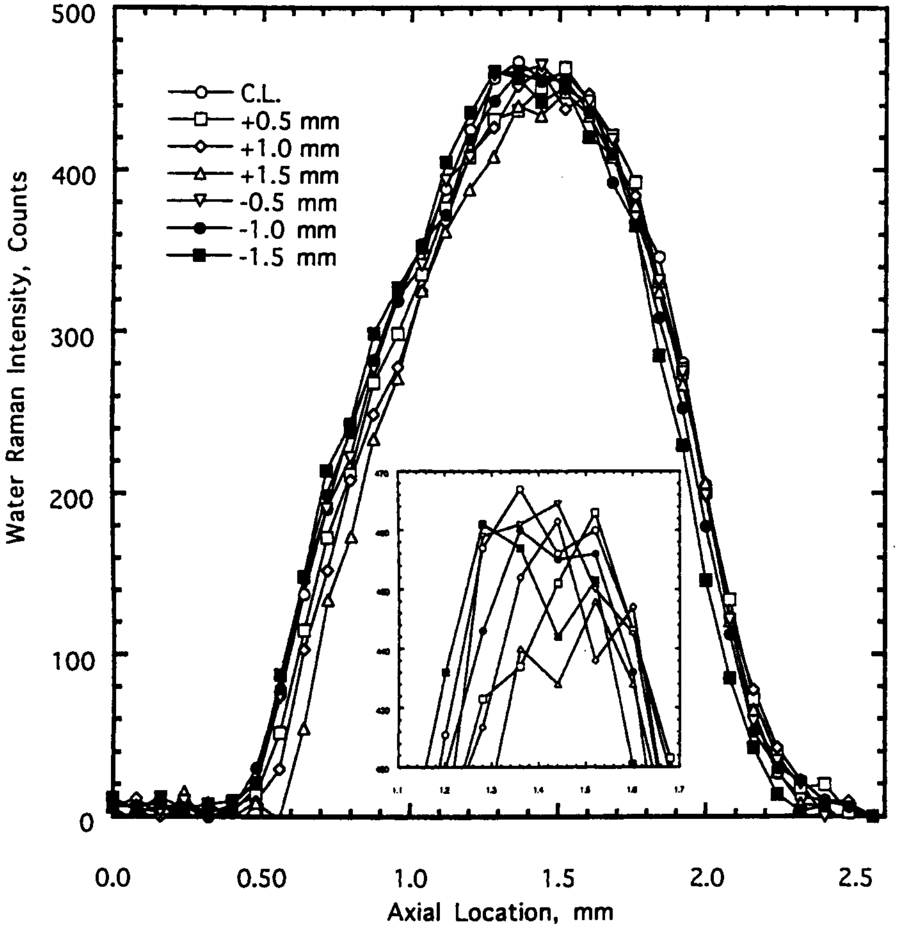

Fig.35 Transverse water Raman profiles versus hydrogen mixture fraction: X_{H2}=0.5, X_{N2}=0.5 a=1250 s^{-1}.

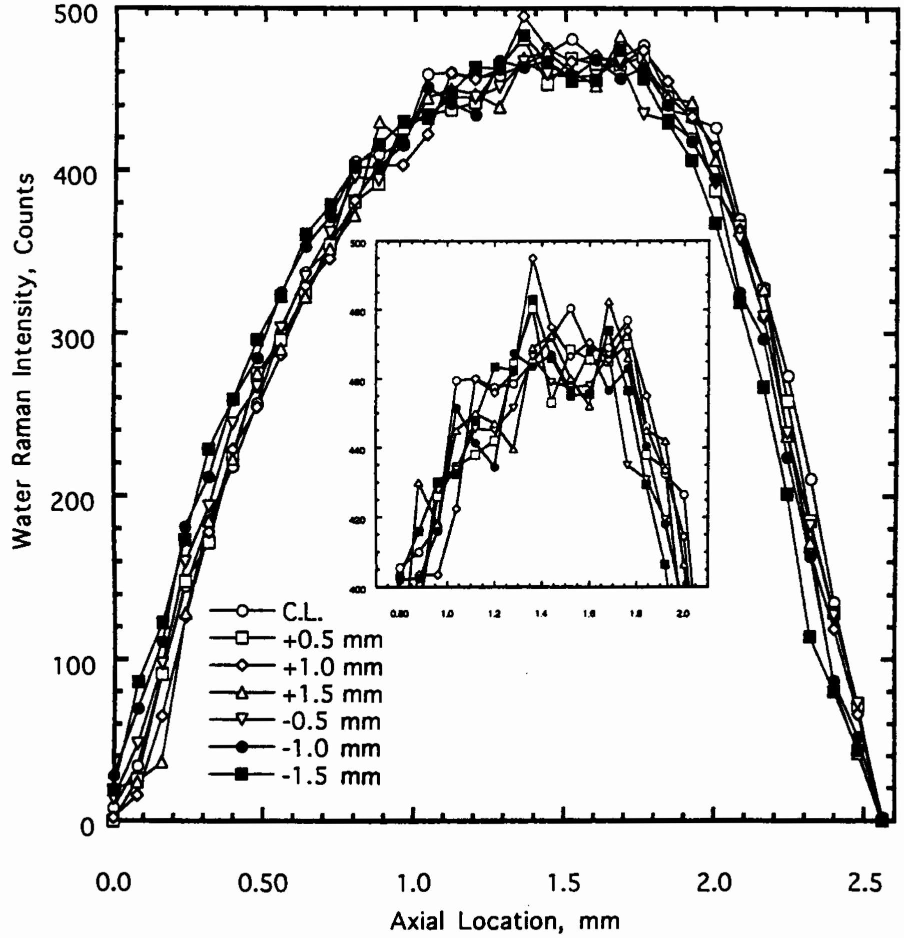

Fig.36 Transverse water Raman profiles versus hydrogen mixture fraction: $X_{H2}=1.0$ $a=604\ s^{-1}$.

APPENDIX-D

MULTICOMPONENT DIFFUSION COEFFICIENTS

Scalar dissipation rate is calculated according to Eq.4-5. This equation requires a calculation of elemental hydrogen diffusion coefficient. To calculate diffusion coefficient of elemental hydrogen into a mixture of combustion species, diffusion coefficient of molecular hydrogen and water vapor into the combustion gases are calculated first. Multicomponent diffusion coefficients of hydrogen and water are calculated by the following equation across the flame zone:

$$D_{km} = \frac{1 - X_k}{\sum\limits_{j \neq k}^{K} \left(X_j / D_{jk} \right)} \qquad \text{(D-1)}$$

where D_{km} is the diffusion coefficient of species k into a mixture, X_k is the mole fraction of species k, and D_{jk} is the binary diffusion coefficient of every specie and specie k. Binary diffusion coefficients are extracted from CHEMKIN transport package and calculated according to the following equation [Kee et al. 1990]:

$$\ln D_{jk} = \sum_{n=1}^{N} d_{n,jk} (\ln T)^{n-1} \qquad \text{(D-2)}$$

where $d_{n,jk}$ represents binary diffusion coefficient curve-fit constants that are calculated by CHEMKIN, and T represents temperature. The error associated with the binary diffusion coefficient curve-fit is indicated to be 2.872E-3 by CHEMKIN output.

After multicomponent diffusion coefficients of molecular hydrogen and water are calculated, simple mole averaging is used to derive at atomic hydrogen multicomponent diffusion coefficient:

$$D_{H,Mix} = \frac{X_{H_2} D_{H_2,Mix} + X_{H_2O} D_{H_2O,Mix}}{X_{H_2} + X_{H_2O}} \qquad \text{(D-3)}$$

An alternative method suggests to calculate elemental hydrogen multicomponent diffusion coefficient as a mole weighted average of binary diffusion coefficients of combustion gases into nitrogen [Nandula, Brown and Pitz 1994; Bilger 1980]. This less accurate method ignores the composition of actual gas mixture and estimates the multicomponent diffusion coefficient as a mole weighted average of binary diffusion coefficients of each species into nitrogen. Comparison of elemental hydrogen multicomponent diffusion coefficient obtained by these two methods is best demonstrated by Fig.37. In this figure ratio of elemental hydrogen multicomponent diffusion coefficients that are calculated by the method outlined above to the diffusion coefficients that are calculated by the method suggested by Bilger is graphed as a function of hydrogen mixture fraction for the equimolar and undiluted fuel jet opposed jet flames of Fig.29 and Fig.30. It is observed that the ratio of multicomponent diffusion coefficient obtained by the two different methods may vary by as much as factor of three at the lean conditions. At lean conditions, Bilger's suggestion results in a diffusion coefficient that is approximately same as nitrogen diffusing into a mixture that is mainly nitrogen. The calculation outlined above gives a value that is approximately three times higher since diffusion coefficient of hydrogen is about three times higher than that is of nitrogen. At rich conditions, the two solutions approach unity. The resultant scalar dissipation rate values are linearly dependent on the diffusion coefficient thus they vary by as much as factor of two depending on the method of calculation.

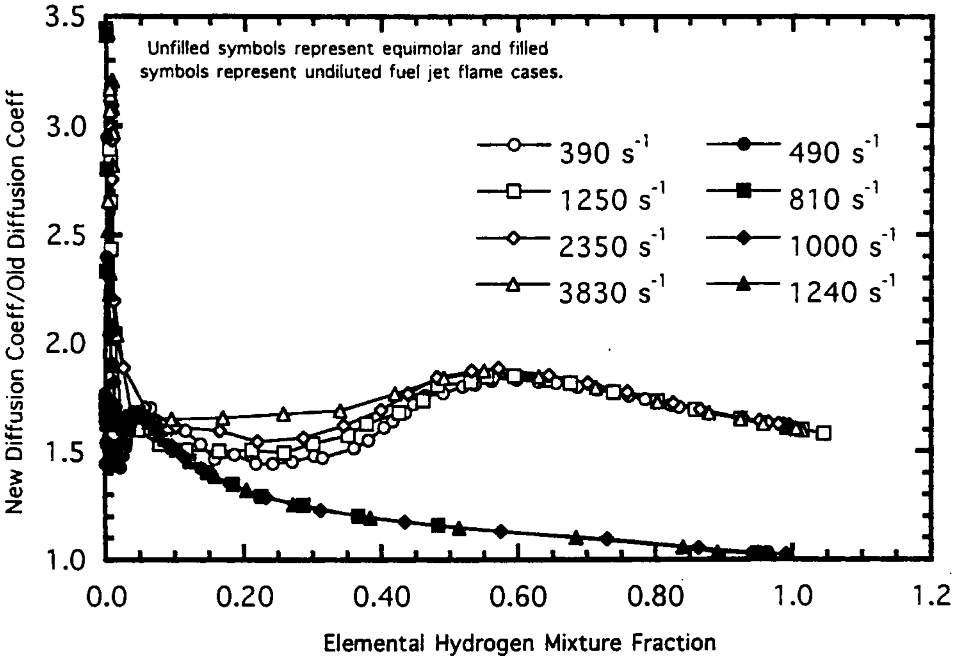

Fig.37 Elemental hydrogen multicomponent diffusion coefficient comparison.

REFERENCES

Anagnostou, E., A. E. Potter. 1963. Flame strength of propane-oxygen flames at low pressures in turbulent flow. In Ninth symposium (international) on combustion, by The Combustion Institute. Pittsburgh, Pennsylvania, 1-6.

Balakrishnan, G., M. D. Smooke, F. A. Williams. 1995. A numerical investigation of extinction and ignition limits in laminar nonpremixed counterflowing hydrogen-air streams for both elementary and reduced chemistry. Combustion and Flame 102: 329-340.

Balakrishnan, G., D. Trees, F. A. Williams. 1994. An experimental investigation of strain-induced extinction of diluted hydrogen-air counterflow diffusion flames. Combustion and Flame 98: 123-126.

Barlow, R. S., C. D. Carter. 1994. Raman/Rayleigh/LIF measurements of nitric oxide formation in turbulent hydrogen jet flames. Combustion and Flame 97: 261-280.

Barlow, R. S., R. W. Dibble, D. C. Fourguette. 1989. Departure from chemical equilibrium in a lifted hydrogen flame. Sandia Report SAND 89-8627, Sandia National Laboratories, Livermore, California.

Barlow, R. S., J.-Y. Chen. 1992. On transient flamelets and their relationship to turbulent methane-air jet flames. In Twenty-fourth symposium (international) on combustion, by The Combustion Institute. Pittsburgh, Pennsylvania, 231-237.

Bilger, R. W. 1980. Molecular transport effects in turbulent diffusion flames at moderate Reynolds number. In AIAA Journal 20: 962-970.

Brown, T. M., S. P. Nandula, P. A. Skaggs, R. W. Pitz, G. L. Pellet, W. Roberts, L.G. Wilson, K.M. Isaac. 1994. Multi-point measurement of temperature and species concentrations in opposed jet flames by UV Raman scattering. AIAA paper 9400226 presented at the 32nd Aerospace Sciences Meeting and Exhibit. Reno, Nevada, 10-13 January.

Chelliah, H. K., C. K. Law, T. Ueda, M. D. Smooke, F. A. Williams. 1990. An experimental and theoretical investigation of the dilution, pressure and flow-field effects on the extinction condition of methane-air-nitrogen diffusion flames. In Twenty-third symposium (international) on combustion, by The Combustion Institute. Pittsburgh, Pennsylvania, 503-511.

Cheng, T. S., J.A. Wehrmeyer, and R.W. Pitz. 1992. Simultaneous temperature and multispecies measurements in a lifted hydrogen diffusion flame. Combustion and Flame 91: 323-345.

Darabiha, N. 1992. Transient behaviour of laminar counterflow hydrogen-air diffusion flames with complex chemistry. Combustion Science and Technology 86: 163-181.

Darabiha, N., S. Candel. 1992. The influence of temperature on extinction and ignition limits of strained hydrogen-air diffusion flames. Combustion Science and Technology 86: 667-85.

Dibble, R., A. R. Masri, and R. W. Bilger. 1987. The spontaneous Raman scattering technique applied to nonpremixed flames of methane. Combustion and Flame 67: 189-206.

Dixon-Lewis, G., T. David, P. H. Gaskell. 1986. Structure and properties of methane-air and hydrogen-air counterflow diffusion flames. Archivum Combustionis 6: 3-21.

Dixon-Lewis, G., and M. Missaghi. 1988. Structure and extinction limits of counterflow diffusion flames of the hydrogen-nitrogen mixtures in air. In Twenty-second symposium (international) on combustion, by The Combustion Institute. Pittsburgh, Pennsylvania, 1461-1470.

Drake, Michael C., M. Lapp, and C. M. Penney. 1982. Use of vibrational Raman effect for gas temperature measurements. In Temperature: Its measurements and control in science and industry, ed. J. F. Schooley, vol. 5. New York: American Institute of Physics, 631-638.

Eckbreth, A., P.A. Bonczyk, and J.F. Verdieck. 1979. Combustion diagnostics by laser Raman and fluorescence techniques. Progress in Energy and Combustion Science 5: 253-32.

Egolfopoulos, F. N. 1994. Dynamics and structure of unsteady, strained, laminar premixed flames. In Twenty-fifth symposium (international) on combustion, by The Combustion Institute. Pittsburgh, Pennsylvania, 1365-1373.

Fendell, F. 1965. Ignition and extinction in combustion of initially unmixed reactants. Journal of Fluid Mechanics 21:281-303.

Gutheil, E., and F.A. Williams. 1990. A numerical and asymptotic investigation of structures of hydrogen-air diffusion flames at pressures and temperatures of high-speed combustion. In Twenty-third symposium (international) on combustion, by The Combustion Institute. Pittsburgh, Pennsylvania, 513-521.

Im, H. G., J. K. Bechtold, C. K. Law. 1995. Counterflow flames with unsteady strain rates. AIAA paper 950128 presented at the 33rd Aerospace Sciences Meeting and Exhibit. Reno, Nevada, 9-12 January.

Im, H. G., C. K. Law, J. S. Kim, F. A. Williams. 1995. Response of counterflow diffusion flames to oscillating strain rates. Combustion and Flame 100: 21-30.

Katta, V. R., W. M. Roquemore. 1995. On the structure of a stretched/compressed laminar flamelet-influence of preferential diffusion. Combustion and Flame 100:61-70.

Kee, R. J., G. Dixon-Lewis, J. Warnatz, M. E. Coltrin, J. A. Miller. 1990. A fortran computer code package for the evaluation of gas-phase multicomponent transport properties. Sandia Report SAND 86-8246, Sandia National Laboratories, Livermore, California.

Kee, R. J., J.A. Miller, G.H. Evans, and G. Dixon-Lewis. 1988. A computational model of the structure and extinction of strained, opposed flow, premixed methane-air flames. In Twenty-second symposium (international) on combustion, by The Combustion Institute. Pittsburgh, Pennsylvania, 1479-1494.

Kim, J.S., F.A. Williams. 1993. Structures of flow and mixture-fraction fields for counterflow diffusion flames with small stoichiometric mixture fractions. American Journal of Applied Mathematics, Vol. 53, No. 6:1551-1566.

Kuo, K. K. 1986. Principles of Combustion. New York: John Wiley & Sons.

Kreutz, T. G., M. Nishioka, C. K. Law. 1994. The role of kinetic versus thermal feedback in nonpremixed ignition of hydrogen versus heated air. Combustion and Flame 99: 758-766.

Lapp, M., C. M. Penney, J. A. Asher. 1973. Application of light scattering techniques for measurements of density, temperature and velocity in gas dynamics. General Electric Co. Schenectady, New York. NTIS, AD-759575.

Law, C. K., C. J. Sung, G. Yu, R. L. Axelbaum. 1994. On the structural sensitivity of purely strained planar premixed flames to strain rate variations. Combustion and Flame 98: 139-154.

Lederman, S. 1977. The use of laser Raman diagnostics in flow fields and combustion. Progress in Energy and Combustion Science 3: 1.

Li, S. C., N. Ilincic. Influences of sprays on strained partially premixed flames. AIAA paper 952555 presented at the AIAA/ASME/SAE/ASEE 31st Jet Propulsion Conference. San Diego, California, 10-12 July.

Liñán, A. 1974. The asymptotic structure of counterflow diffusion flames for large activation energies. Acta Astronautica 1: 1007-1039.

Lommel, E. 1878. Wiedemanns Annalen 3: 251.

Luna, R. E. 1965. A study of impinging axi-symmetric jets and their application to size classification of the small particles. Ph.D. diss., Princeton University.

Muss, J. A., R. W. Dibble, L. Talbot. 1994. A helium-hydrogen mixture for the measurement of mixture fraction and scalar gradient in non-premixed reacting flows. AIAA paper 940612 presented at the 32nd Aerospace Sciences Meeting and Exhibit. Reno, Nevada, 10-13 January.

Nandula, S. P., T. M. Brown, R. W. Pitz. 1994. Measurements of scalar dissipation in the reaction zones of turbulent nonpremixed H_2-air flames. Combustion and Flame 99: 775-783.

Nandula, S. P., T. M. Brown, R. W. Pitz, P. A. DeBarber. 1994. Single-pulse, simultaneous multipoint, multispecies Raman measurements in turbulent nonpremixed jet flames. Optics Letters 19:414-416.

Nicholls, E. L. 1900. Physical Review 10:234-252.

Pandya, T. P., and F. J. Weinberg. 1964. The structure of flat, counter-flow diffusion flame. Proceedings of Royal the Society of London 279: 544-561.

Papas, P., I. Glassman, and C.K. Law. 1994. Effects of pressure and dilution on the extinction of counterflow nonpremixed hydrogen-air flames. In Twenty-fifth symposium (international) on combustion, by The Combustion Institute. Pittsburgh, Pennsylvania, in press.

Pellett, G. L., G. B. Northam, L. G. Wilson. 1992. Strain-induced extinction of hydrogen-air counterflow diffusion flames: effects of steam, CO_2, N_2, and O_2 additives to air. AIAA paper 920877 presented at the 30th Aerospace Sciences Meeting and Exhibit. Reno, Nevada, 6-9 January.

Pellett, G. L., G. B. Northam, L. G. Wilson, W. M. Humphreys, S. M. Bartram, L. R. Gartrell, K. M. Isaac. 1995. Velocity fields of axisymmetric hydrogen-air counterflow diffusion flames from LDV, PIV, and numerical computation. AIAA paper 953112 presented at the 31st Joint Propulsion Conferences. San Diego, California, 10-12 July.

Pellett, G. L., G.B. Northam, L.G. Wilson, O. Jarrett Jr., R.R. Antcliff, C.L. Dancey, and J.A. Wang. 1989. Opposed jet diffusion flames of nitrogen-diluted hydrogen vs air: axial LDA and CARS surveys; fuel/air strain rates at extinction. AIAA paper 892522 presented at the AIAA/ASME/SAE/ASEE 25th Joint Propulsion Conference. Monterey, California, 10-12 July.

Peters, N. 1984. Laminar diffusion flamelet models in non-premixed turbulent combustion. Progress in Energy and Combustion Science, 10:319-339.

Peters, N. 1986. Laminar flamelet concepts in turbulent combustion. In Twenty-first symposium (international) on combustion, by The Combustion Institute. Pittsburgh, Pennsylvania, 1231-1250.

Placzek, G. 1934. Rayleigh-streuung und Raman effekt. In Handbuch der Radiologie, Heft 6, Teil 2, ed. Erich Marx. Leipzig: Akademische Verlag. [The Rayleigh and Raman scattering]. 1962. Washington: Office of Technical Services, Department of Commerce, NTIS, UCRL-Trans-526(L).

Plath, I., W. Meier, W. Stricker. 1992. Application of a backside-illuminated charge-coupled-device camera for single-pulse coherent anti-Stokes Raman spectroscopy N_2 thermometry. Optics Letters 17:79-81.

Potter, A. E., J. N. Butler. 1959. Journal of American Rocket Society 29: 54-56.

Potter, A. E., S. Heimel, J. N. Butler. 1962. Apparent flame strength: A measure of maximum reaction rate in diffusion flames. In Eight symposium (international) on combustion, by the Combustion Institute. Pittsburgh, Pennsylvania, 1027-1034.

Prandtl, L. 1904. Verhandlg. III Intern. Math. Kongr. Heidelberg, 484-491.

Puri, I. K., K. Seshadri. 1986. Extinction of diffusion flames burning diluted methane and diluted propane in diluted air. Combustion and Flame 65:137-150.

Raman, C. V. 1928. Indian Journal of Physics 2: 387.

Raman, C. V., S. Krishnan. 1928. Nature 501.

Reckers, W., L. Hüwel, G. Grünefeld, P. Andresen. 1993. Spatially resolved multispecies and temperature analysis in hydrogen flames. Applied Optics 32: 907-918.

Reynolds, W. C. 1986. STANJAN chemical equilibrium solver, v. 3.30 IBM-PC (C), Stanford University.

Rolon, J. C., F. Aguerre, S. Candel. 1995. Experiments on the interaction between a vortex and a strained diffusion flame. Combustion and Flame 100: 422-429.

Rolon, J. C., D. Veynante, J.P. Martin, F. Durst. 1991. Counter jet stagnation flows. In Experiments in Fluids , ed. N. Peters and B. Rogg, New York: Springer-Verlag, 11: 313-324.

Schlichting, H. 1955. Boundary Layer Theory. New York: McGraw-Hill.

Sick, V., A. Arnold, E. Dießel, T. Dreier, W. Ketterle, B. Lange, J. Wolfrum, K. U. Thiele, F. Behrendt, J. Warnatz. 1990. Two-dimensional laser diagnostics and modeling of counterflow diffusion flames. In Twenty-third symposium (international) on combustion, by The Combustion Institute. Pittsburgh, Pennsylvania, 495-501.

Smekal, A. 1923. Naturwissenschaften. 11:873.

Smooke, M.D., I. K. Puri, K. Seshadri. 1988. A comparison between numerical calculations and experimental measurements of the structure of a counterflow diffusion flame burning diluted methane in diluted air. In Twenty-first symposium (international) on combustion, by The Combustion Institute. Pittsburgh, Pennsylvania, 1783-1792.

Spalding, D. B. 1961. Theory of mixing and chemical reaction in the opposed-jet diffusion flame. Journal of American Rocket Society 31: 763-771.

Tangirala, V., K. Seshadri, C. Treviño, M. D. Smooke. 1990. Analysis of the structure of counterflow hydrogen-air diffusion flames. In Dynamics of Deflagrations and Reactive Systems: Flames, ed. A. R. Seebass, vol. 133. Washington D.C.: Progress in Astronautics and Aeronautics, 89-110.

Trees, D., T.M. Brown, M. D. Smooke, K. Seshadri, R. W. Pitz, G. Balakrishnan, V. Giovangigli, S. P. Nandula. 1995. The structure of nonpremixed hydrogen-air flames. Combustion Science and Technology, 104: 427-432.

Tsuji, H., and I. Yamaoka. 1966. The counterflow diffusion flame in the forward stagnation region of a porous cylinder. In Eleventh symposium (international) on combustion, by The Combustion Institute. Pittsburgh, Pennsylvania, 979-983.

Tsuji, H., A. Yoshida, N. Endo. 1994. Effect of turbulence on extinction of counterflow diffusion flame. In Twenty-fifth symposium (international) on combustion, by The Combustion Institute. Pittsburgh, Pennsylvania, 1191-1197.

Wehrmeyer, J. A., S. Yeralan, K. S. Tecu. 1995a. Multispecies Raman imaging in flames by use of an unintensified charge-coupled device. Optics Letters 20: 934-936.

Wehrmeyer, J. A., S. Yeralan, K. S. Tecu. 1995b. Linewise Raman-Stokes/anti-Stokes temperature measurements in flames using an unintensified charge-coupled device. Applied Physics B 61: in press.

Yaney, P. P., R.J. Becker, P.D. Magill, and P. Danset. 1982. Dynamic temperature measurements of flames using spontaneous Raman scattering. In Temperature: Its measurements and control in science and industry, ed. J. F. Schooley, vol. 5. New York: American Institute of Physics, 639-648.

Yeo, S. H., and C.L. Dancey. 1991. Experimental determination of the velocity and strain rate field in a laminar H_2/air counter-flow diffusion flame via LDA. In Fourth conference (international) on laser anemometry, by ASME. Cleveland, Ohio, 121-129.

Zhao, J., K. M. Isaac. 1995. Nitric oxide formation in strained H_2-air diffusion flames. AIAA paper 950132 presented at the 33rd Aerospace Sciences Meeting and Exhibit. Reno, Nevada, 9-12 January.

VITA

Serdar Yeralan was born October 18, 1966, in Ankara, Turkey. After graduating from public high school, he moved to the United States of America to enroll in Mechanical and Aerospace Engineering Department at University of Missouri-Columbia. He earned his B.S. in Mechanical Engineering in May, 1989 and immediately pursued M.S. degree at University of Wisconsin-Madison in the area of combustion science. After completing his degree in 1991, he decided to go back to University of Missouri-Columbia and study hydrogen combustion using laser diagnostics with Dr. Wehrmeyer. After completion of his Ph.D., he is now currently working with Dr. Santoro at Pennsylvania State University, Propulsion Engineering Research Center.

University Bindery, Inc.
St. Louis, MO 5-99